Short-term corrosion behavior of 316 stainless steel in molten salt LiCl–KCl–$CaCl_2$ as high temperature thermal storage medium

Le Zhao[1], Baorang Li[1], Xiaoze Du[1,2†], Hongwei Wu[3]

1 Key Laboratory of Power Station Energy Transfer Conversion and System (North China Electric Power University), Ministry of Education, Beijing 102206, China

2 School of Energy and Power Engineering, Lanzhou University of Technology, Lanzhou 730050, China

3 School of Physics, Engineering and Computer Science, University of Hertfordshire, Hatfield, AL109AB, UK

Abstract

The effects of alkaline earth metal salts on the corrosion of Fe-Cr alloys are not clear up to now. The ternary chloride salts are the potential high-temperature thermal energy storage medium for future application. In this study, the short-term corrosion behavior of two ternary chloride salts LiCl–KCl–$CaCl_2$ with different content $CaCl_2$ on 316 stainless steel (316 SS) are investigated by immersion experiments at 650 ℃. The effect of $CaCl_2$ content on the formation and evolution of corrosion products are revealed by the kinetics, microstructure and chemical analysis of corroded 316 SS. Meanwhile, the effects of 316 SS before and after corrosion on salt chemistry and thermal properties are also characterized by ICP-OES and infrared spectroscopy, respectively. The results indicate that the dissolution of Fe-Cr into the ternary chloride salt cannot change the chemical properties of the

† Corresponding author. Tel.: +86(10)61773923; Fax: +86(10)61773877. Email address: duxz@ncepu.edu.cn (X. Du)

ternary chloride salt LiCl–KCl–$CaCl_2$. However, the dissolution of Fe-Cr reduces the melting temperature of ternary chloride salts LiCl–KCl–$CaCl_2$. These findings provide new ideas for molten salts design and corrosion control for high-temperature thermal energy storage medium of concentrated solar power.

Keywords: Ternary chloride salts; 316 stainless steel; chemical analysis; corrosion

1. Introduction

Thermal energy storage (TES) can solve the intermittent problem of concentrated solar power (CSP) [1]. The present high-temperature tower CSP deploys nitrate salts as TES medium [2]. The decomposition of nitrate salts at high temperatures is limited to 565 ºC [3]. Higher temperature TES medium with chloride salts attract numerous attentions recently to make CSP more competitive in the future [4, 5]. The main reasons for choosing chloride salt are its low cost and low melting temperature [6]. However, chloride salts are highly corrosive to structural alloys at high temperatures [7-11]. It is a key factor hindering large-scale commercial use of molten chloride salts [12, 13].

The influence and mechanism of molten salt on structural materials have been paid much attention by many scholars [14-20]. The high-temperature corrosion behavior of 310H stainless steel (SS) at 750 ºC in air, with different NaCl–Na_2SO_4 ratios, is discussed by Tsaur et al. [14]. NaCl is considered to be the main corrosive medium and the cause of internal corrosion. The metal oxide film reacts with molten NaCl or KCl. Subsequently, the protective oxide film is destroyed. When alkali metal chromate reacts with NaCl, a liquid substance with a low onset temperature is formed. The liquid material accelerates the corrosion process through the capillary action of the oxide film. The effect of thermal aging on the corrosion behavior of 316H SS in high-temperature molten salt NaCl–KCl–$MgCl_2$ is studied by Li et al. [15]. The relationship between microstructure/precipitates and corrosion behavior is discussed. Moreover, it is aimed at the hot corrosion of oxide or chloride film. Wang et al. [16] conduct corrosion tests of 316 stainless steel (316 SS) in NaCl–KCl–NaF interactive salt at different temperatures. The results show that low oxygen-containing acidity is beneficial to the formation of stable chromium oxides. Liu et al. [8] study the three nickel-based alloys of Inconel 625, Hastelloy and Hastelloy B-3 alloys in NaCl–$CaCl_2$–$MgCl_2$ molten salt at 600 ºC. The corrosion test

results show that the corrosion resistance of Inconel 625 alloy with high Cr-Ni content in NaCl–$CaCl_2$–$MgCl_2$ molten salt is better than that of Hastelloy and Hastelloy B-3 alloys in air. Xu et al. [17] simulate the corrosion behavior of Fe-Cr-Ni alloy in NaCl–$CaCl_2$ molten salt by using two-dimensional cellular automata method. The detailed changes and migration rules of each component with time during the corrosion process of Fe-Cr-Ni alloy in molten chloride salt are revealed. The simulation results show that the element composition and the content of O_2 and H_2O in the molten salt are the important factors that significantly affect the corrosion resistance of Fe-Cr-Ni alloy in NaCl–$CaCl_2$ molten salt. This result can provide new directions for molten salt design and corrosion control. Therefore, in this study, two ternary chloride salts with different ratios is designed to detect their corrosion behavior on matrix.

Meanwhile, some studies have shown that the structural alloys are corroded and dissolved by the chloride salts at high temperatures. Then, the elements generated by structural alloys enter the high-temperature chloride salts melt [18, 19]. Pure alkali and alkaline earth metal chlorides do not cause corrosion of the alloy in principle. Oxidative impurities in the molten chloride salts such as non-molten metal ions (Cr^{3+}, Fe^{2+}, Fe^{3+}, Ni^{2+}), gases and oxides covered in the air are the main causes of structural alloys corrosion [20]. However, some researchers hold different views, and they think alkali metal chlorides exist in molten. These structural alloys are likely to undergo hot corrosion even at a moderate temperature [21, 22].

It is well known that high-temperature molten chloride salt aggravates the corrosion of structural alloys, such as 316 SS. The reason for this result is that there may be multiple competition mechanisms. The overall increase in corrosion rate does not necessarily mean that each mechanism accelerates corrosion. The mechanism and its relative strength inevitably change in different working

fluids [23]. Some studies have shown that corrosion atmosphere [24] and oxide/hydroxide impurities [25] can affect the selective dissolution of chromium in chloride molten salts. Wang et al. [12] consider the combined effect of dissolution and chlorination of alloys in molten chlorides. When the alloy is exposed to air, the oxygen and water in the air are continuously dissolved in the molten chloride and reacted with the molten chloride to form corrosive HCl and Cl_2. These corrosive impurities can accelerate the corrosion of structural alloys, especially the Cr element in structural alloys. For 316 SS, the oxide-based passivation does not occur, because its corrosion products and common protective oxides are soluble in high-temperature molten salt [7]. Thus, 316 SS corrosion in high-temperature molten salt is different from that in a wet environment [26]. The main corrosion mechanism of nickel-based structural alloy in high temperature molten salts is the selective dissolution of the most sensitive elements such as chromium into the molten salt [23]. Net loss of atoms is caused by dissolution and corrosion of structural alloy surface. This causes voids on the surface of the structural alloy [27]. The distribution of voids is generally considered to be local and distributed along grain boundaries [28].

The ternary chloride salts LiCl–KCl–$CaCl_2$ have broad operating temperatures and high energy storage densities. However, the corrosion of the structural alloy caused by chloride salts limited their application in the new generation high-temperature CSP [29-32]. Especially for alkaline earth metals salt such as $CaCl_2$, it easily absorbs water in the air and then formed $CaCl_2 \cdot n(H_2O)$. After heating, $CaCl_2 \cdot n(H_2O)$ decomposed to produce CaO, leading to the content change of $CaCl_2$ in the mixed molten salt. Meanwhile, it cannot be ruled out whether the hydrolysis process affected the corrosion of the structural alloy. Whether the alkaline earth metal salt content affects the corrosion of structural alloys is unclear up to now. In addition, most of researches focus on the corroded substrate, and few

pay attention to the molten salt after work.

Therefore, the purpose of this study is to investigate the corrosion behavior of Fe-based structural alloy (316 SS) in different contents of $CaCl_2$ in ternary chloride salts under the air. The effect of the alkaline earth metal salts on the corrosion behavior of 316 SS will be evaluated. Meanwhile, the effect of 316 SS corrosion on molten salt is studied. The corrosion behavior is studied according to the mass change, chemical composition and microstructure analysis of 316 SS after corrosion. The chemical analysis and thermal properties of the related salt are characterized by Inductively Coupled Plasma Optical Emission Spectroscopy (ICP-OES), infrared spectroscopy and differential scanning calorimeter before and after corrosion. The main purpose is to clarify the effect of alkaline earth metal salt $CaCl_2$ content on the corrosion performance of 316 SS. The relationship between the content of alkaline earth metal salts, the chemistry of the ternary chloride salts and the corrosion of the structural alloy are established. These results can provide new ideas for the design and corrosion control of molten salts.

2. Experiments and methodology

2.1. Materials preparation and test procedure

Unpurified chloride salts (LiCl, KCl and $CaCl_2$) are purchased from Shanghai Macklin and selected for the preparation of the ternary chloride salts. Two kinds of different ternary chloride salts LiCl–KCl–$CaCl_2$ are made. The ratio of the ternary chloride LiCl–KCl–$CaCl_2$ is obtained based on the phase diagram calculated by FactSage. Based on Factsage, LiCl–KCl–$CaCl_2$ corresponded to three melting temperatures of 340.93, 433.57 and 626.85 ºC, respectively, and the corresponding components are 37.85-53.38-8.77, 30.90-13.82-55.28 and 1.78-18.61-79.61 wt. %. However, melting

temperature of the third group of salts is too high, so only the first two groups of salts are considered. Then, we test the melting temperature and maximum operating temperature by Differential scanning calorimeter and synchronous thermal analyzer. The results show that the melting temperature and maximum operating temperature of salt 1 is 342.51 ºC and 652.0 ºC. The melting temperature and maximum operating temperature of salt 2 is 426.44 ºC and 695.5 ºC. The composition of ternary chloride salts LiCl–KCl–$CaCl_2$, melting temperature and maximum operating temperature of the two salts are listed in Table 1.

Table 1. The component of ternary chloride salts LiCl–KCl–$CaCl_2$, melting temperature and thermal stabilities of the two salts.

Ternary chloride salts	Samples	Component	Melting temperature	Maximum operating temperature under air
		wt. %	ºC	ºC
LiCl–KCl–$CaCl_2$	Salt 1	37.85-53.38-8.77	342.51	652.0
	Salt 2	30.90-13.82-55.28	426.44	695.5

The composition of the 316 stainless steel (316 SS) is listed in Table 2. Before the corrosion experiment, 316 SS samples with dimensions of 8.0 mm × 8.0 mm × 3.0 mm were cleaned with distilled water, acetone and ethyl alcohol. Then, the 316 SS is dried b cooled air.

Table 2. Chemical compositions of 316 SS (wt%).

Element	Fe	Cr	Ni	Mo	Mn	Cu
Content	69.20	16.73	10.61	1.96	1.19	0.187

Salt 1 and salt 2 are assembled in different crucibles in order to accurately reflect the corrosion kinetics of two ternary chloride salts on 316 SS. Then, the supports under the lid are used to make the two ternary chloride salts fully contact with the air to maintain the chemical stability of the salt, as shown in Fig.1. The static immersion test is carried out in a muffle furnace at 650 ºC, and the temperature is controlled with an accuracy of ± 1 ºC. 20.0 g solid ternary chloride salts LiCl–KCl–$CaCl_2$ is added into the Al_2O_3 crucible. The 316 SS sample is completely immersed in high-temperature liquid molten salt to ensure that 316 SS fully contacts with the molten salt during the corrosion experiment. The 316 SS is taken out from the crucible after 24 h, 48 h and 72 h, respectively. The samples are washed with deionized water to remove the residual molten salt. After cleaning the sample, the aqueous solution is collected for composition analysis. The corrosion samples after cleaning are used to evaluate the corrosion behavior of the ternary chloride salts LiCl–KCl–$CaCl_2$.

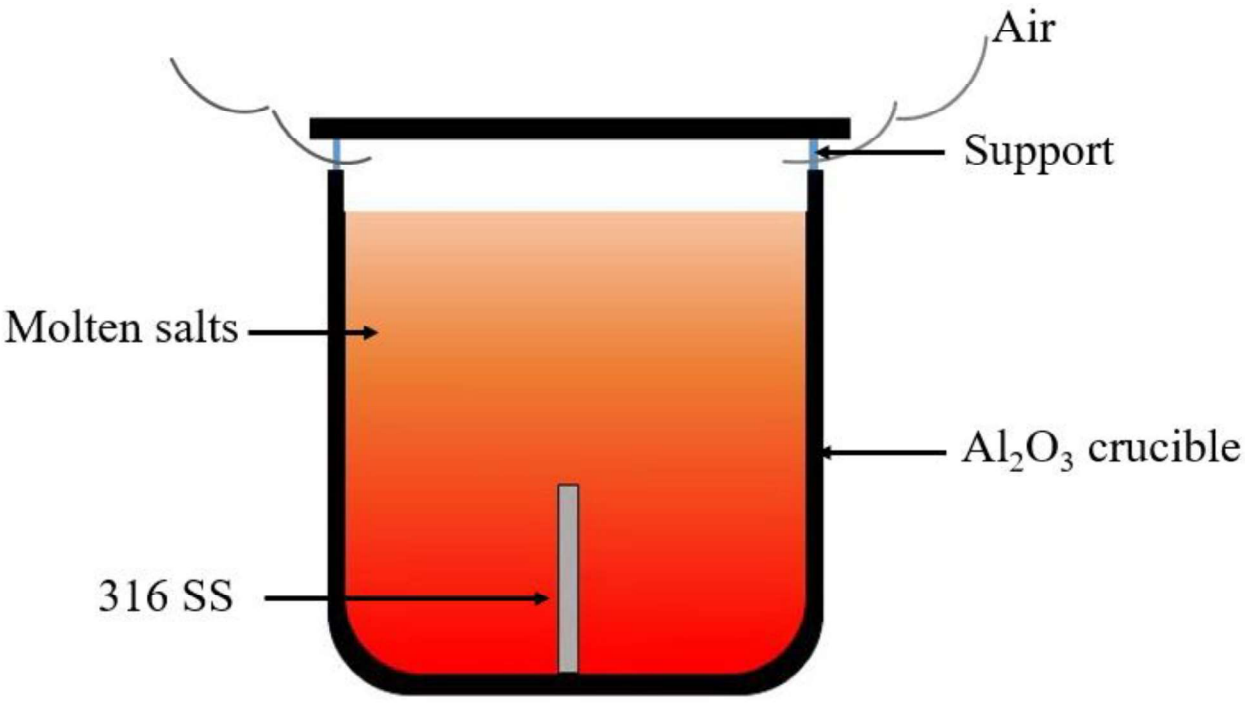

Fig.1. Apparatus of the static immersion test.

2.2. Surface characterization of the corrosion product scales

The mass loss is used to define the corrosion rate of 316 SS to evaluate the effect of two different ternary chloride salts LiCl–KCl–$CaCl_2$. The sample is washed with deionized water in order to maintain the maximum integrity of the sample (especially the surface oxide film). Fig.2 shows the macroscopic corrosion morphology of 3166 SS exposed to two different ternary chloride salts. The weight of 316 SS at each stage is measured using an accurate electronic balance (accuracy 0.1 mg). Mass loss of 316 SS after corrosion, average corrosion rate and equivalent corrosion depth of 316 SS can be calculated by Eq.(1), (2) and (3), respectively [33, 34].

$$M = (m_1 - m_2)/S \quad (1)$$

$$R = M/t \quad (2)$$

$$D = M/\rho \quad (3)$$

where, m_1 is initial weight, m_2 is the weight after corrosion and cleaning; M is descaled mass loss of corrosion sample per unit area over time (g/cm^2); ρ (g/cm^3) is the density of 316 SS; S is the initial area of the specimen in cm^2; D (μm) is equivalent corrosion depth.

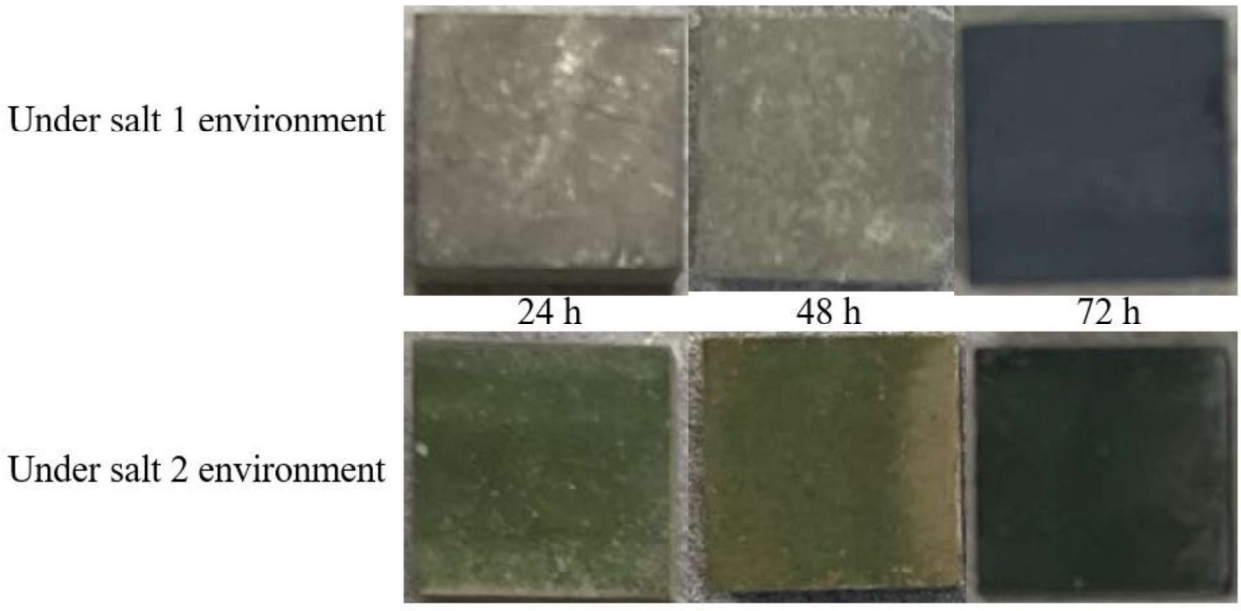

Fig.2. Macro-morphologies of 316 SS after corrosion at 650 ºC for different time.

2.3. Chemical analysis and thermal properties of ternary chloride salts LiCl–KCl–$CaCl_2$ before and after corrosion

ICP-OES is used to detect the concentration of Fe and Cr elements dissolved in the ternary chloride salt. Additionally, pure salts such as LiCl, KCl, $CaCl_2$ and ternary chloride salts LiCl–KCl–$CaCl_2$ before and after corrosion are analyzed by infrared spectroscopy to determine the chemical composition and structure of the salts. To determine whether the ternary chloride salt has chemical changes during the corrosion of 316 SS, the Frontier FT-IR/NIR spectrometer is used to collect the infrared spectra of ternary chloride salts before and after corrosion of 316 SS. The samples used for infrared spectroscopy are ground into powder in an agate mortar and then smeared on a diamond window. The melting temperature of ternary chloride salt before and after corrosion is characterized by Differential Scanning Calorimetry (DSC 3, Mettler Toledo).

2.4. Microstructure of 316 SS before and after corrosion

Scanning electron microscope (SEM; Zeiss Merlin FE) and Energy Dispersive Spectrometer (EDS; oxford Instruments X-Max 80 mm^2) are used to characterize the morphology and element distribution of the corroded 316 SS. The corrosion rate of 316 SS in salt 1 increased first and then decreased slowly with the immersion time. The crystalline corrosion products are characterized by X-ray diffractometer (XRD). The active area of Cu Kα ray is 10 mm × 10 mm, the test range was 2θ = 10-90º, and the step length is 0.02º/s.

3. Results and analysis

Two sorts of samples of ternary chloride salts LiCl–KCl–$CaCl_2$, salt 1 and salt 2, described in Table 1 are used for corrosion tests in the present study. The corrosion kinetics of 316 SS can give an indication of the corrosion mechanism [35]. Since the experiment is carried out in an air atmosphere, the ternary chloride salts exposed to different $CaCl_2$ contents have a significant effect on the corrosion of 316 SS. The mass changes of 316 SS exposed to two salt environments at 650 ºC are shown in Fig.3. All structural alloys show a decrease in quality. When 316 SS is exposed to salt 1 environment, the weight loss of 316 SS is only 0.041 mg/cm^2 in the first 24 h, and the corrosion is highly slight. As a comparison, 316 SS exposed to salt 2 environment is more corrosive. The weight loss of 316 SS is 0.549 mg/cm^2. However, it is found that the weight loss of 316 SS exposed to salt 2 decrease with time.

The corrosion rate diagram can indicate the corrosion mechanism. In order to analyze the effect of corrosion products on the corrosion rate of 316 SS, Fig.4 shows the average corrosion rate of 316 SS in two ternary chlorides with different $CaCl_2$ contents. All structural alloys show a tendency that the 316 SS is corroded. As shown in Fig.4, compared with that in salt 2, the average corrosion rate of 316 SS in the first 24 h under salt 1 immersion is 0.041 mg/cm^2·h. The corrosion rate of 316 SS in salt 1 increases first and then decreases slowly with the immersion time. This result is consistent with the existing literature [8]. While 316 SS is immersed under salt 2 environment, 316 SS shows a strong corrosion rate of 0.549 mg/cm^2·h in the first 24 h. The corrosion rate decreases with the extension of immersion time. This indicates that the growth of corrosion layer is controlled by the solid diffusion growth process, which can provide a protective behavior, and the dissolution rate of corrosion products in molten salt is limited.

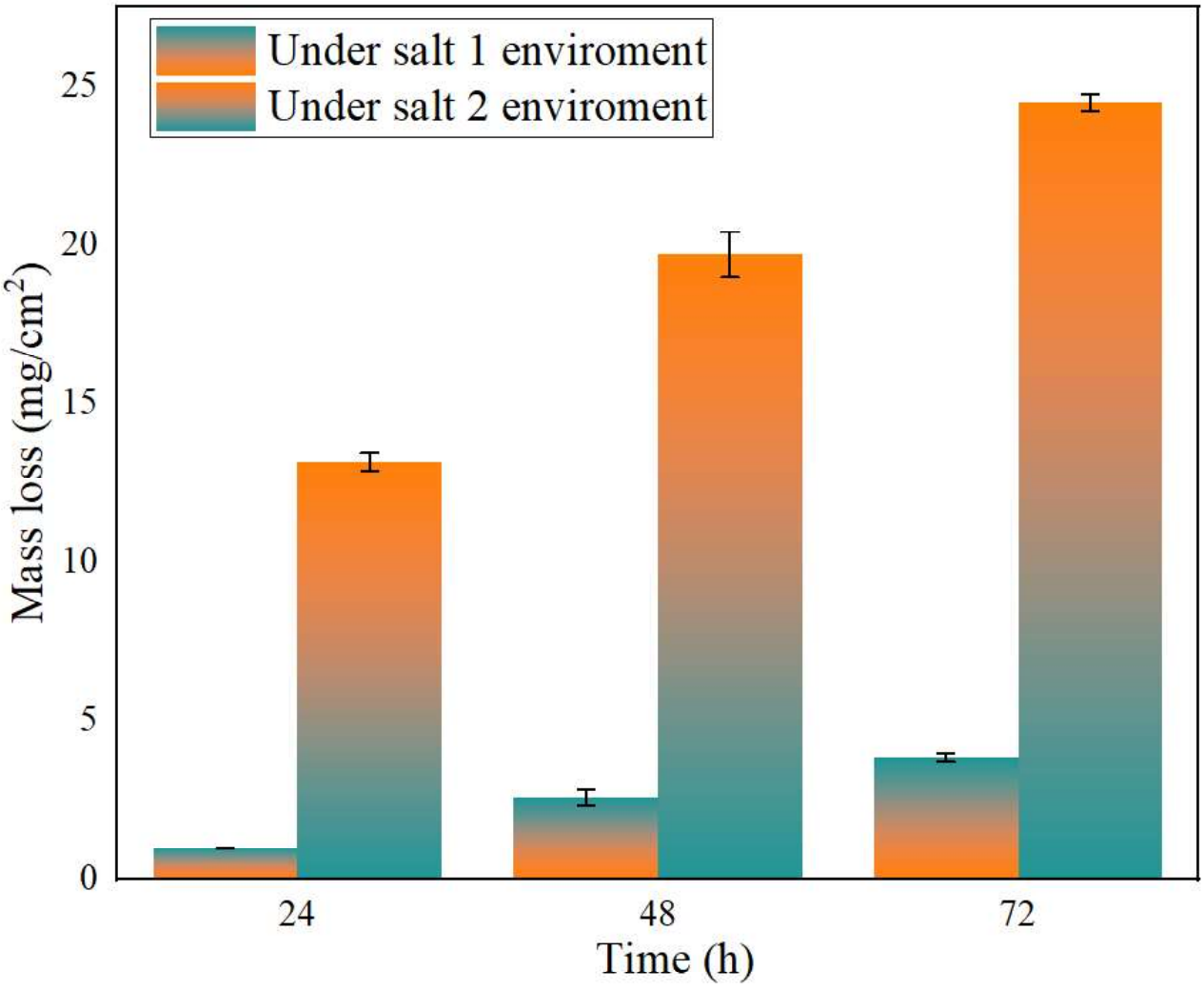

Fig.3. Mass loss of 316 SS immersed in different component ternary chloride salts LiCl–KCl–$CaCl_2$ for different time.

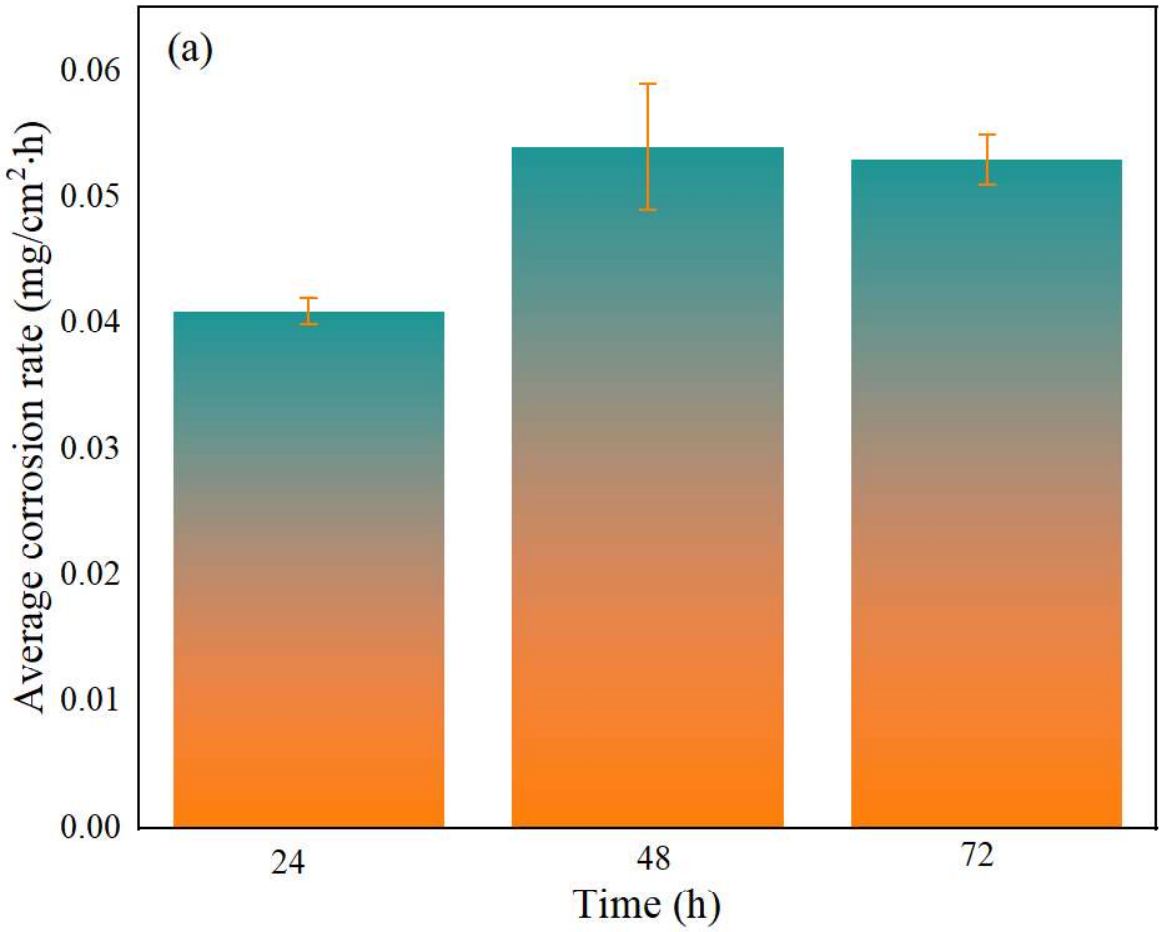

(a) The average corrosion rate of 316 SS under salt 1 environment.

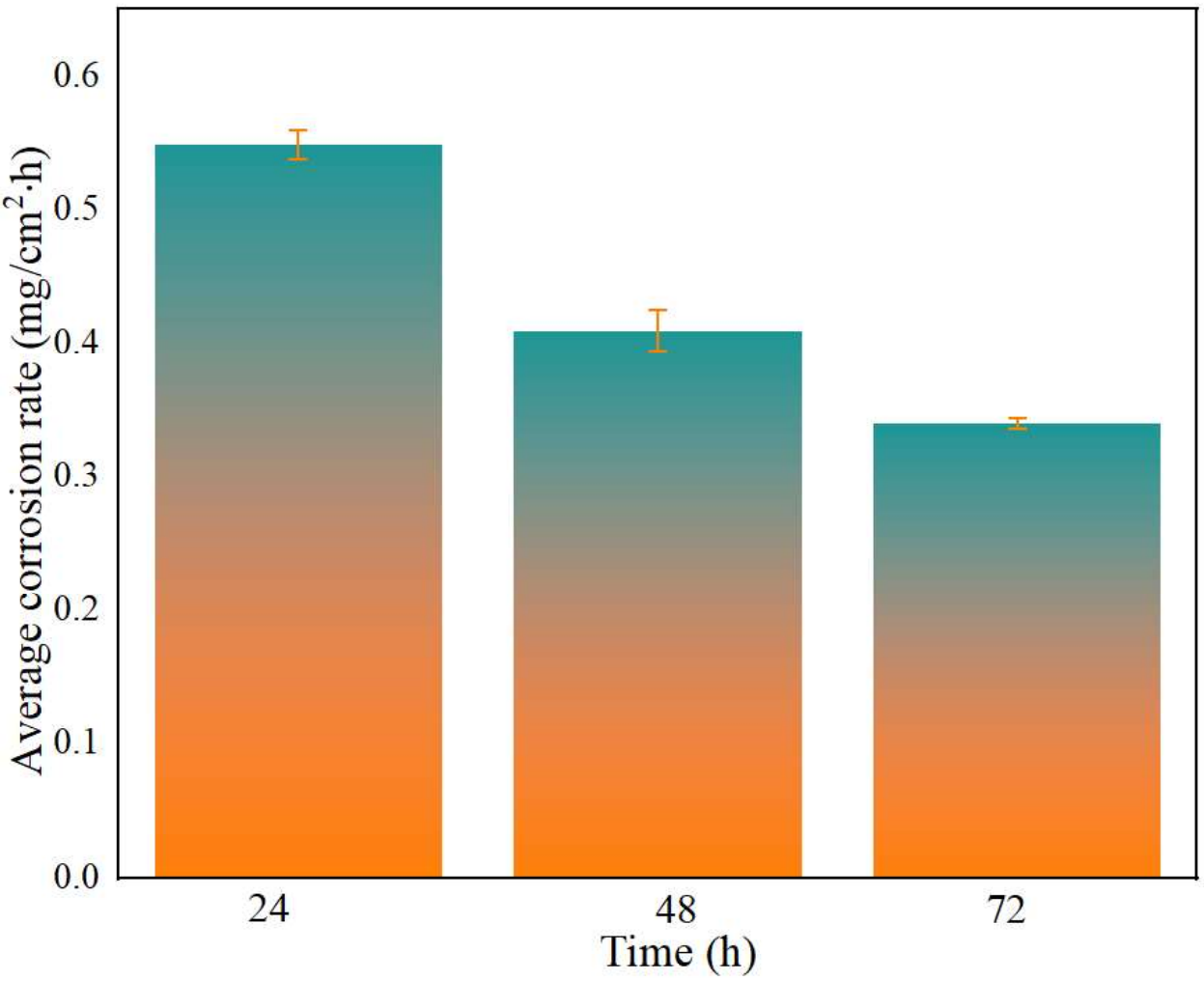

(b) The average corrosion rate of 316 SS under salt 2 environment.

Fig.4. The average corrosion rate of 316 SS in different compositions of ternary chloride salt LiCl–KCl–$CaCl_2$ at different times.

The corrosion rate of 316 SS is determined by the equivalent depth. The corrosion degree of 316 SS in ternary chlorides with different contents of $CaCl_2$ with time is quantitatively analyzed. The equivalent corrosion depth of 316 SS is calculated by Eq.(4), as shown in Fig.5. It can be found that with the extension of time, the equivalent corrosion depth gradually deepens, but the corrosion rate decreases. It should be noted that the corrosion rate increases within 48 h in the salt 1 environment. This is because the thickness and density of the corrosion products are not enough to protect the matrix.

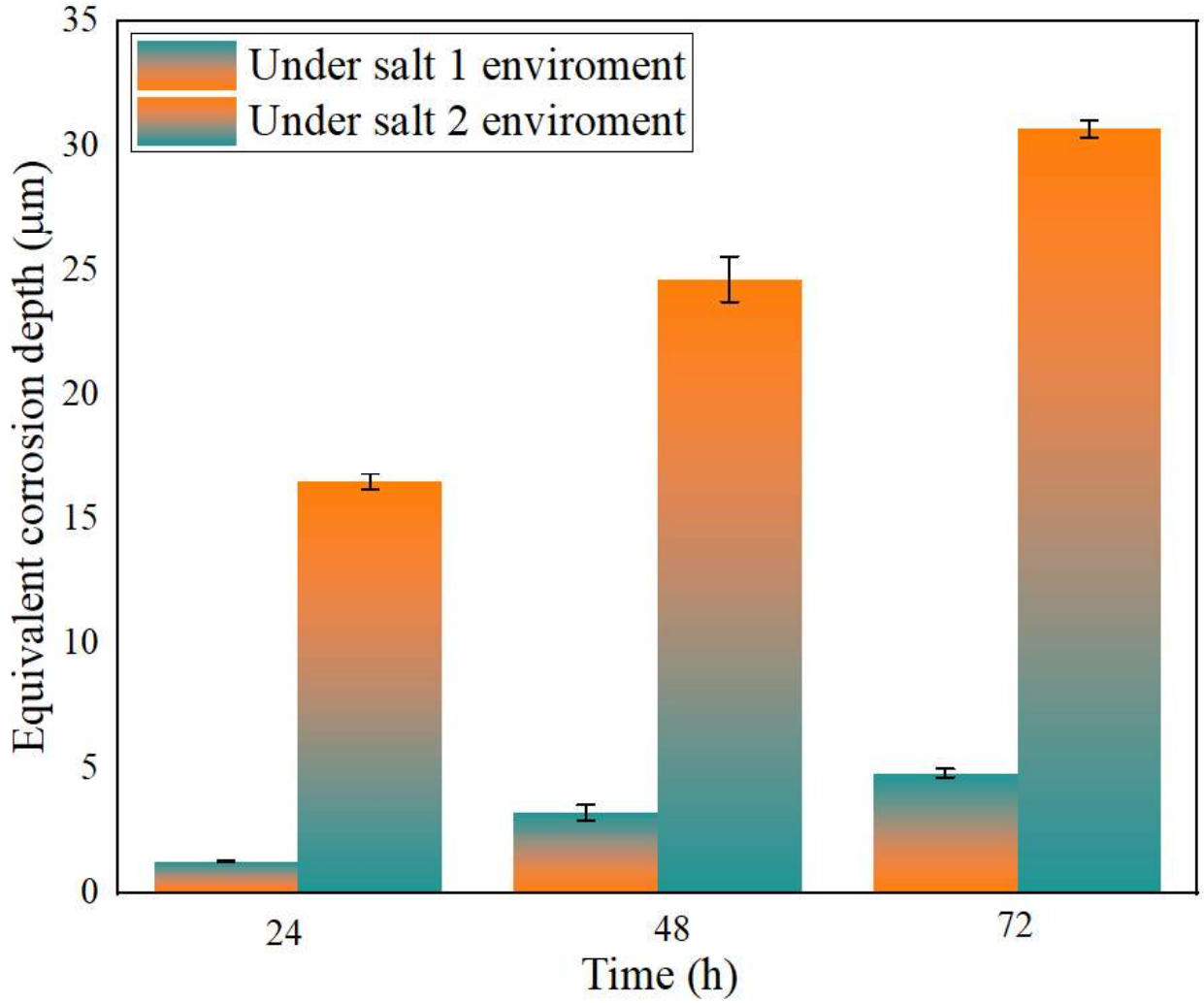

Fig.5. The equivalent corrosion depth of 316 SS.

In addition, to clarify the relationship between the equivalent corrosion depth and the average corrosion rate of 316 SS, the mass loss of 316 SS after corrosion, the corrosion rate and the equivalent corrosion depth of the 316 SS are summarized in Table 3. It can be found that the average corrosion rate of 316 SS decrease with the increase of equivalent corrosion depth. Although the equivalent corrosion depth can reflect the corrosion degree of 316 SS, it cannot reflect the cross-section corrosion characteristics of the sample directly. Therefore, Fig.6 further confirms that the dense corrosion layer

can reduce the corrosion rate of 316 SS when the outer corrosion layer reaches a certain thickness and there is no intergranular corrosion. Fig.6 shows the cross-section morphology of 316 SS after immersion in chloride salts with different $CaCl_2$ contents in air for 24, 48 and 72 h. Under the ternary chloride salt, 316 SS is divided into three layers and they are the top layer, the middle layer and the bottom layer (outer corrosion layer, inner corrosion layer and matrix). Under salt 2 environment, there is obvious intergranular corrosion in the outer corrosion layer. This is because the energy at the grain boundary is higher, which is easier to dissolve and react. This intergranular corrosion rapidly penetrates into the metal matrix, resulting in the thickness of the inner corrosion layer of 316 SS in the salt 2 environment being significantly thicker than that in the salt 1 environment. This finding directly indicates that once intergranular corrosion occurs in the outer corrosion layer, the corrosion products continue to penetrate deep into the metal matrix. No obvious grain boundary corrosion is observed in 316 SS under salt 1 environment.

Table 3. Mass loss of 316 SS after corrosion, average corrosion rate and equivalent corrosion depth of 316 SS under different components for different time.

Component	Time	Mass loss		Corrosion rate	Equivalent corrosion depth
	h	mg	mg/cm^2	$mg/cm^2 \cdot h$	μm
Salt 1	24	2.20	0.982	0.041	1.231
	48	5.80	2.589	0.054	3.244
	72	8.60	3.839	0.053	4.811
Salt 2	24	29.50	13.170	0.549	16.504
	48	44.10	19.688	0.410	24.672
	72	54.90	24.509	0.340	30.713

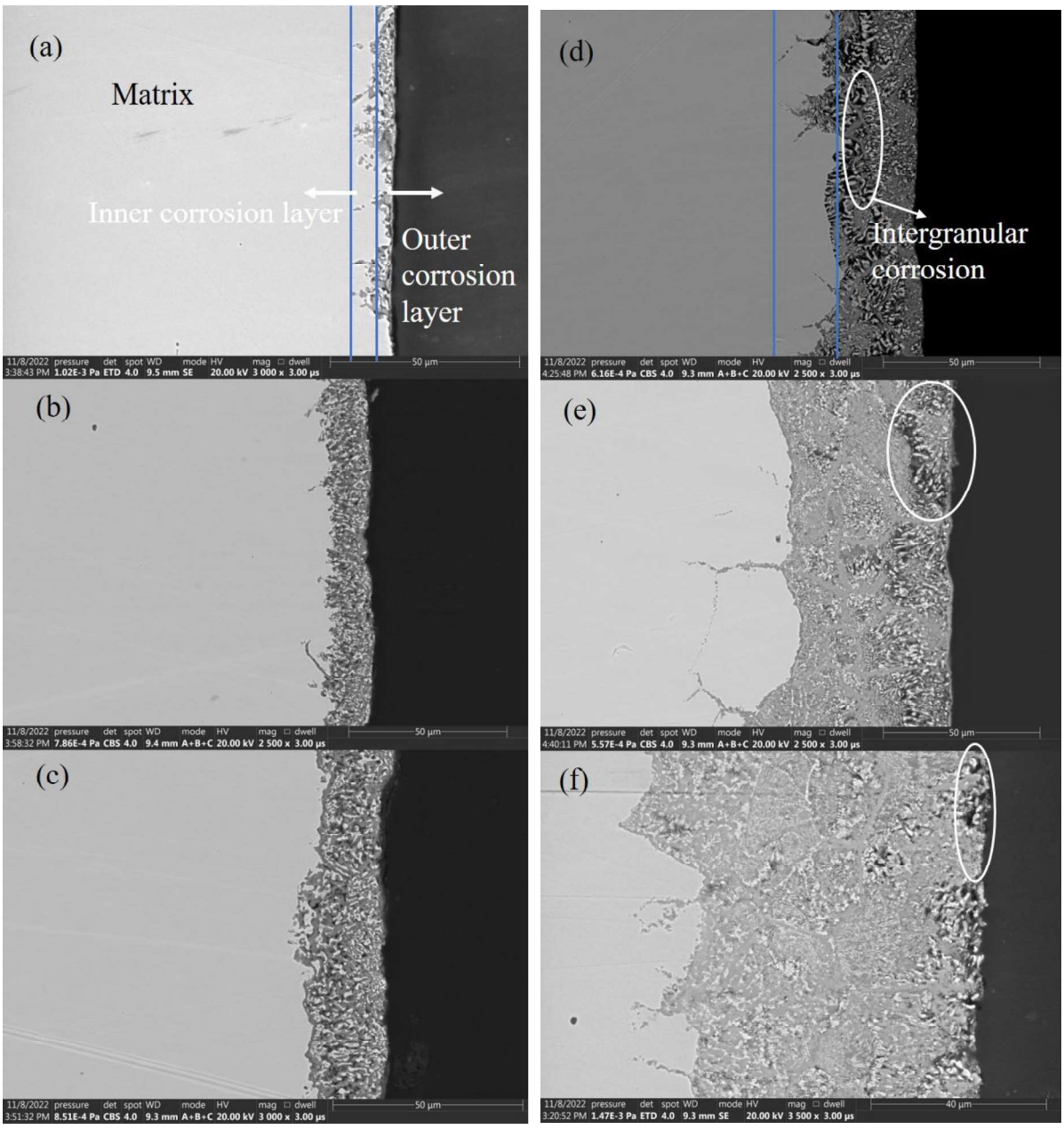

Fig.6. SEM images of the corroded 316 SS in ternary chloride salts LiCl–KCl–$CaCl_2$ with different content of $CaCl_2$ at 650 ºC for different time. (a) 316 SS corroded for 24 h under salt 1 environment; (b) 316 SS corroded for 48 h under salt 1 environment; (c) 316 SS corroded for 72 h under salt 1 environment; (d) 316 SS corroded for 24 h under salt 2 environment; (e) 316 SS corroded for 48 h under salt 2 environment; (f) 316 SS corroded for 72 h under salt 2 environment.

4. Discussion of corrosion mechanism

4.1 Salt analysis

The two ternary chloride salts show white before corrosion of 316 SS, and gradually become gray with the extension of corrosion time. From the appearance color, the color of salt 2 after corrosion of 316 SS is obviously darker than that of salt 1, as shown the microscopic diagram of Fig.7. In order to further confirm this conclusion, the Fe-Cr elements in the molten salt before and after corrosion of 316 SS are tested by ICP-OES, and the results are shown in Table 4. The experimental results show that the content of Fe and Cr in salt 2 after corrosion of 316 SS is much higher than that in salt 1. Furthermore, the Fe element in salt 1 and salt 2 after corrosion of 316 SS is higher than the Cr element, indicating that Fe is more easily dissolved in ternary chloride than Cr. This result is consistent with the characterization results in Fig.7. There is "Fe deficiency and Cr enrichment" in the outer corrosion layer.

Experiments show that the intergranular corrosion of Fe-Cr structural alloy caused by molten chloride salts LiCl–KCl–$CaCl_2$ is highly dependent on salt chemistry [36, 37]. However, these studies have not found the effect of alkaline earth metal $CaCl_2$ on the solubility of Fe-Cr structural alloy, because of the very low solubility of Cr. Microanalysis results of Fig.10 show that the corrosion of 316 SS in molten ternary chloride salts was mainly attributed to the dissolution of Fe. 316 SS immersed in salt 2 even appeared to partial dissolution of Cr. Therefore, the compactness of corrosion products produced by 316 SS under salt 1 environment was much greater than that under salt 2 environment. The solubility of Fe-Cr in salt 2 was much higher than that of Salt 1, which further indicated that $CaCl_2$ has certain solubility for Cr. Ternary chloride salts LiCl–KCl–$CaCl_2$ with more alkaline earth metal $CaCl_2$ content are more corrosive to 316 SS. The reason for this result may be the strong water absorption of $CaCl_2$, which leads to the introduction of more impurities and corrosive

gases in ternary chloride salts LiCl–KCl–$CaCl_2$ during the heating process.

Fig.7. Macro-morphologies of ternary chloride salts before and after corrosion conducted at 650 ºC for different time.

Table 4. The content of Fe-Cr element before and after corrosion 316 SS.

Materials	Fe		Cr	
	mg/kg	%	mg/kg	%
Salt 1	16.9	0.0017	0	0
24-Salt 1	80.9	0.0081	5.4	0.0005
48-Salt 1	90.1	0.0090	6.8	0.0007
72-Salt 1	114.0	0.0114	7.0	0.0007
Salt 2	18.5	0.0018	4.6	0.0005
24-Salt 2	259.2	0.0259	8.1	0.0008
48-Salt 2	1045.3	0.1045	19.6	0.0020
72-Salt 2	2658.2	0.2658	36.7	0.0037

To confirm whether Fe-Cr structural alloy dissolved in high-temperature molten salts LiCl–KCl–$CaCl_2$ occurs chemical reaction, the IR of the respective salts and the ternary chloride salts before and after corrosion are characterized. The results are shown in Fig.8. H_2O exhibits different characteristic peaks in the infrared spectra [38, 39]. The infrared spectra of pure NaCl, KCl and $CaCl_2$ are characterized, as shown in Fig.8(a).

The infrared spectra of all ternary chloride salts have obvious wide absorption peaks at 3800 ~ 2750cm^{-1} and small absorption peaks at 1638cm^{-1}, as shown in Fig.8(a), which are the characteristic peaks of H_2O [40]. It can be seen from Fig.8(a) that the infrared spectra of $CaCl_2$ also shows strong absorption peaks at 3425 cm^{-1} and 1637 cm^{-1}, while KCl has no similar peaks. It can be attributed to the layered crystal structure of $CaCl_2$, water can easily penetrate into the $CaCl_2$ crystal to form $CaCl_2.xH_2O$ hydrate. Therefore, the existence of H_2O peak in the infrared spectrum of ternary chloride salts LiCl–KCl–$CaCl_2$ should be attributed to $CaCl_2.xH_2O$. The ternary chloride salt LiCl–KCl–$CaCl_2$ after corroding 316 SS is consistent with the chloride salt before corrosion, and no chemical reaction occurs.

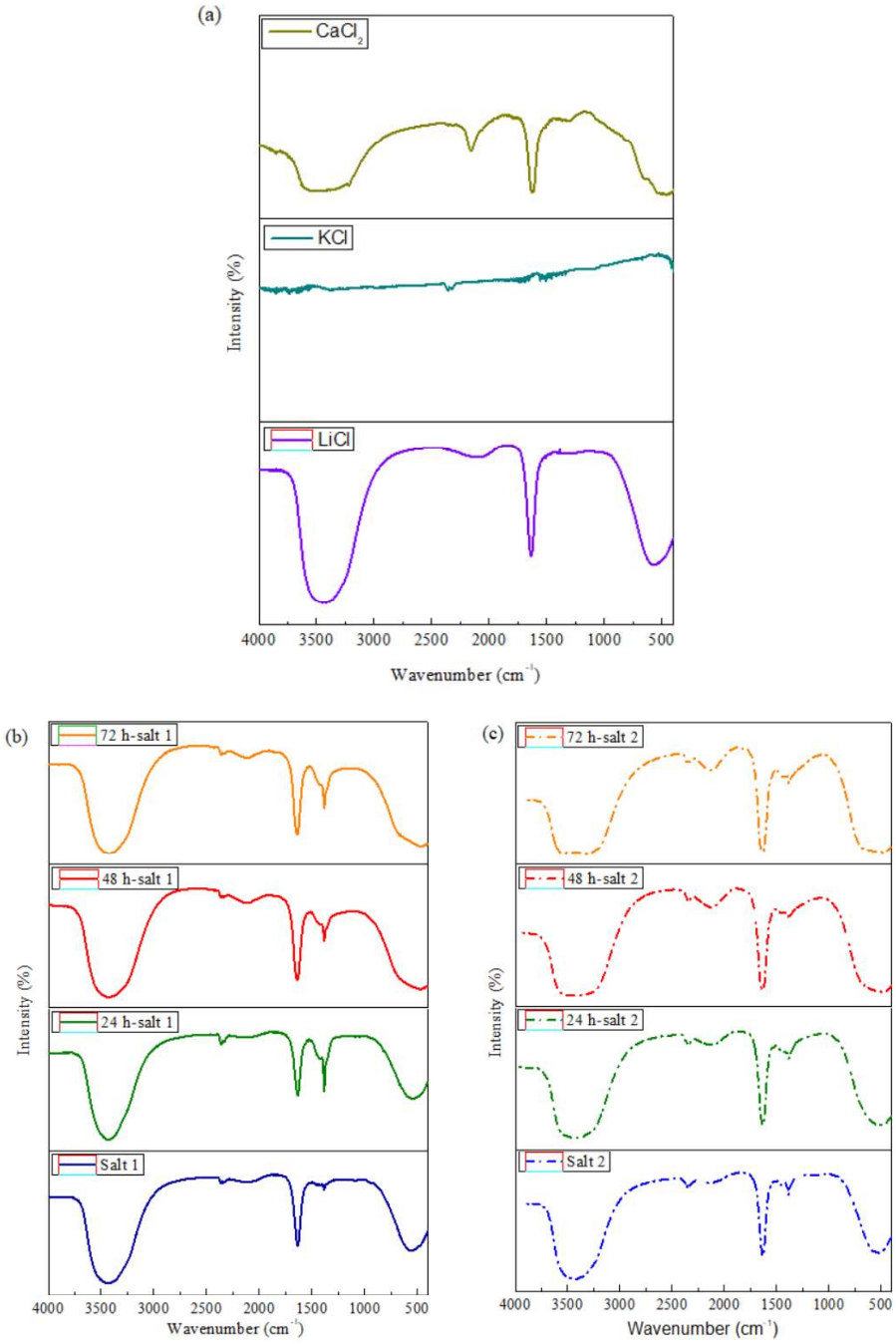

Fig.8. IR spectra of individual chloride salt and ternary chloride salts LiCl–KCl–$CaCl_2$ with different compositions after corrosion. (a) IR spectra of individual chloride salt; (b) Salt 1 before and after corrosion with different time; (c) Salt 2 before and after corrosion with different time.

The dissolution of Fe-Cr in 316 SS inevitably leads to a change in the thermal properties of the ternary chloride salt LiCl–KCl–$CaCl_2$. The phase transition temperatures of the two ternary chloride

salts before and after corrosion are shown in Fig.9. And the specific phase transition temperatures are shown in Table 5. The ternary chloride salt soaked by 316 SS shows three peaks. The corrosion process is carried out under air conditions, so the ternary chloride salt will absorb water during the corrosion process, as indicated in Eq.(4), resulting in a strong water absorption peak at about 100 ºC. $CaCl_2$ undergoes a series of reactions at room temperature, so a series of hydrolysis reactions will occur at 180 ºC. Meanwhile, with the dissolution of Fe-Cr into ternary chloride salt LiCl–KCl–$CaCl_2$, the onset temperature shows a significant downward trend.

$$CaCl_2 \cdot 2\,H_2O + \Delta H \leftrightarrow CaCl_2 + 2H_2O \quad 180\ ^{\circ}C \qquad (4)$$

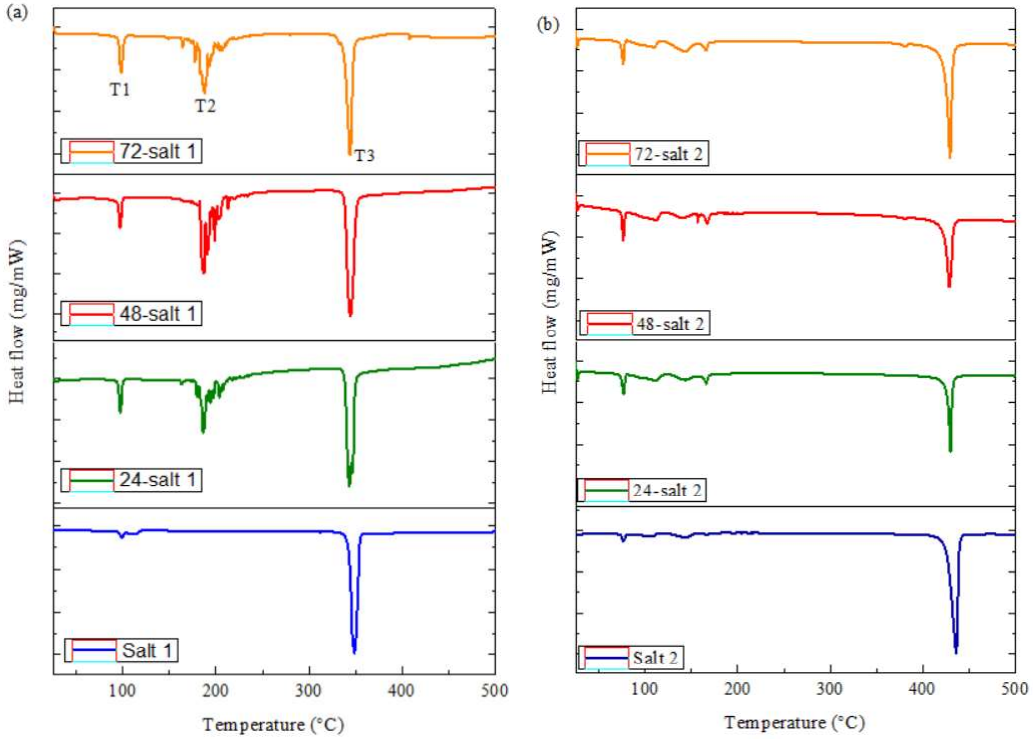

Fig.9. Melting temperatures of ternary chloride salts. (a) Melting temperatures of ternary chloride salts of salt 1 before and after corrosion; (b) Melting temperatures of ternary chloride salts of salt 2 before and after corrosion.

Table 5. Melting temperature of the ternary chloride salts LiCl–KCl–$CaCl_2$ before and after corrosion.

Samples	T_m
	ºC
Salt 1	342.51
24-salt 1	338.47
48-salt 1	338.20
72-salt 1	337.97
Salt 2	426.44
24-salt 2	425.87
48-salt 2	422.87
72-salt 2	423.34

4.2 **Corrosion mechanism**

Cr is considered to be the most corrosive component among Fe, Cr and Ni. It has the strongest chemical reactivity and the fastest diffusion rate in the structural alloy [41, 42]. During the preparation process, the molten salt is only melted at high temperatures without special purification treatment. The molten salt contains corrosive impurities, such as water, oxygen and chloride gas. Therefore, 316 SS may undergo the following reactions when immersed in molten ternary chloride salts LiCl–KCl–$CaCl_2$ with two different contents of $CaCl_2$ [22, 43]. Previous work has shown that when the alloy and molten salt are isolated from air, the corrosion rate of the alloy in molten chloride salt is significantly reduced. When operating in air, oxygen and water vapor will accelerate the corrosion of the alloy in molten salt [8, 31]. According to the Eqs.(5)–(14), after the reaction of O_2 and H_2O, there

will be HCl, Cl_2 and H_2 in the molten salt. In addition, it can be seen from the IR results that $CaCl_2$ has strong water absorption. According to the formula, the higher the content of $CaCl_2$, the more impurities are introduced. Therefore, the higher the content of $CaCl_2$, the more H_2O and O_2 are introduced, resulting in more HCl, Cl_2 and H_2. These corrosive gases enter the molten salt, resulting in more serious corrosion of 316 SS.

$$CaCl_2 + H_2O \rightarrow CaO + 2HCl \quad \text{(molten state)} \tag{5}$$

$$CaCl_2 + H_2O \rightarrow Ca(OH)_2 + 2HCl \quad \text{(infrared radiation+water vapor)} \tag{6}$$

$$4Cl^- + H_2O \rightarrow 2O^{2-} + 2Cl_2 \tag{7}$$

$$2Cl^- + H_2O \rightarrow O^{2-} + HCl \tag{8}$$

$$4HCl_{(g)} + O_{2(g)} \rightarrow 2Cl_{2(g)} + 2H_2O_{(g)} \tag{9}$$

$$Cl_{2(g)} + M_{(g)} \rightarrow MCl_n \tag{10}$$

$$nM_{(s)} + mH_2\,O_{(g)} \rightleftarrows M_nO_{m(s)} + mH_{2(g)} \tag{11}$$

$$nM_{(s)} + (m/2)O_{2(g)} \rightleftarrows M_nO_{m(s)} \tag{12}$$

$$nM_{(s)} + m\,H\,Cl_{(g)} \rightleftarrows M_nCl_{m(s)} + (m/2)H_{2(g)} \tag{13}$$

$$M_nO_{m(s)} + 2mHCl_{(g)} \rightleftarrows M_nCl_{2m} + mH_2O_{(g)} \tag{14}$$

in which, M represents Fe, Cr.

According to the results of Section 3.1, 316 SS is corroded under salt 1 environment slightly, and 316 SS is corroded seriously under salt 2 environment. Therefore, the cross-sectional element distribution of the corrosion layer is further analyzed for 316 SS under two different component molten salts, as shown in Fig.10.

After exposing to salt 1 for 24 h, the surface boundary of 316 SS is no longer smooth. As shown in Fig.6(a), (b) and (c), 316 SS exhibits a continuous outer corrosion layer. The corrosion layer

presents a dense and complete structure. The corrosion layer maintains a good bond with the matrix. From the distribution of Fe, Cr and O elements in Fig.10(a), it can be seen that the top layer is rich in Cr and O elements, and the bottom layer is the structural alloy with local Fe deficiency due to the small selectivity loss of Fe. The Fe of corroded 316 SS completely dissolves in the ternary chloride salts LiCl–KCl–$CaCl_2$. The Cr element is enriched in the corrosion zone to form a protective film. The O element diffuses inward and forms a protective film with Cr. The corrosion layers maintain good bonding with the structural alloy, as shown in Fig.10(a), (b) and (c). Obviously, a dense corrosion protective layer (outer corrosion layer) is formed on the surface of 316 SS. The dense corrosion protective layer prevents the diffusion of corrosive elements to the matrix of 316 SS and the dissolution of Fe element to a certain extent.

When 316 SS are exposed to salt 2 environment, not only a large area of intergranular corrosion appeared in the outer corrosion layer, but also a large area of cracks appeared in the inner corrosion layer, as shown in Fig.10(d), (e) and (f). Fe-poor and Cr-poor phenomenon appears in intergranular corrosion. Furthermore, obvious intergranular corrosion appears along the grain boundary. At the intergranular, Cr and Fe elements in 316 SS structural alloy diffuse outward. Therefore, the corrosion rate of 316 SS under salt 2 environment is much higher than that under salt 1 environment. Combined with the element distribution map of 316 SS corroded under salt 1 environment, it can be seen that the elements in the outer corrosion layer are mainly O and Cr, which is the obvious missing area of Fe. This indicates that Fe is selectively dissolved, accompanied by diffusion, reaction and depletion from the matrix alloy to the molten salt. Net loss of atoms caused by surface dissolution and corrosion of structural alloys. This leads to voids on the surface of structural alloys. The distribution of voids is usually considered to be local and preferentially distributed along grain boundaries.

The surface oxide formed by the outer corrosion layer is dense and compact because less impurities are formed under salt 1 environment. Thus, the surface oxide can protect the oxide from the invasion of the corrosive medium and then form a single type of Cr oxide along the grain boundary. The content of impurity in salt 2 increases, and the thickness of the outer corrosion layer also increases accordingly. Therefore, the internal corrosion layer/matrix is not flat and cracks are common in the oxide layer, due to the continuous deformation caused by impurities. The matrix is also brittle. With the increase of strain, the surface oxides and oxides formed by the outer corrosion layer invade the matrix, and the matrix is further broken. The broken oxide layer and the intrusion provide a channel into the molten salt, which induces further corrosion of the exposed substrate to form an inner corrosion layer. In addition, the dissolution of Cr in the outer corrosion layer leads to the invasion of multilayer oxides.

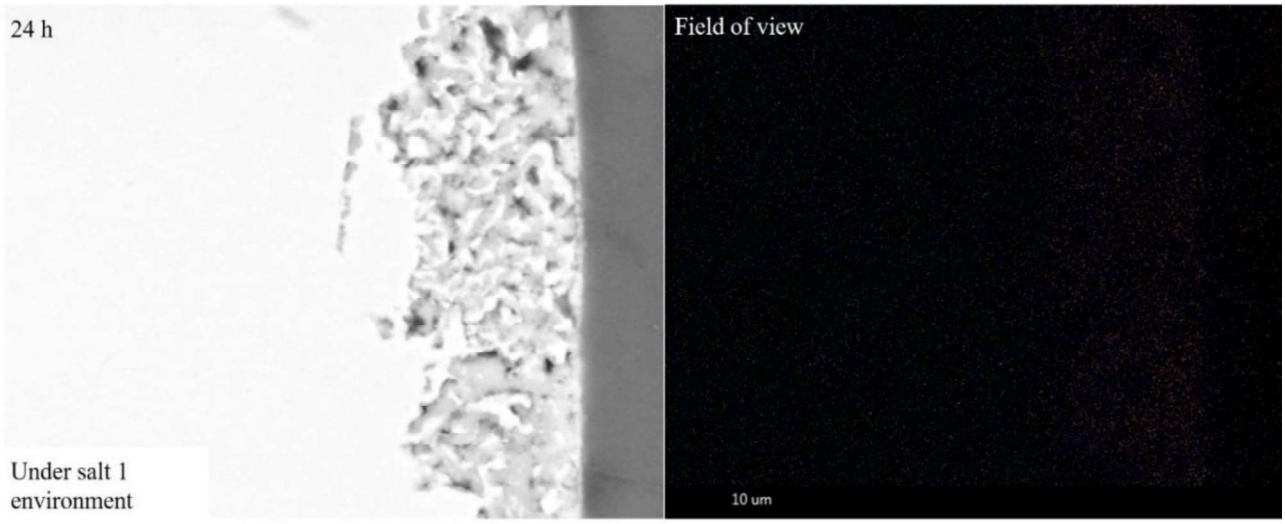

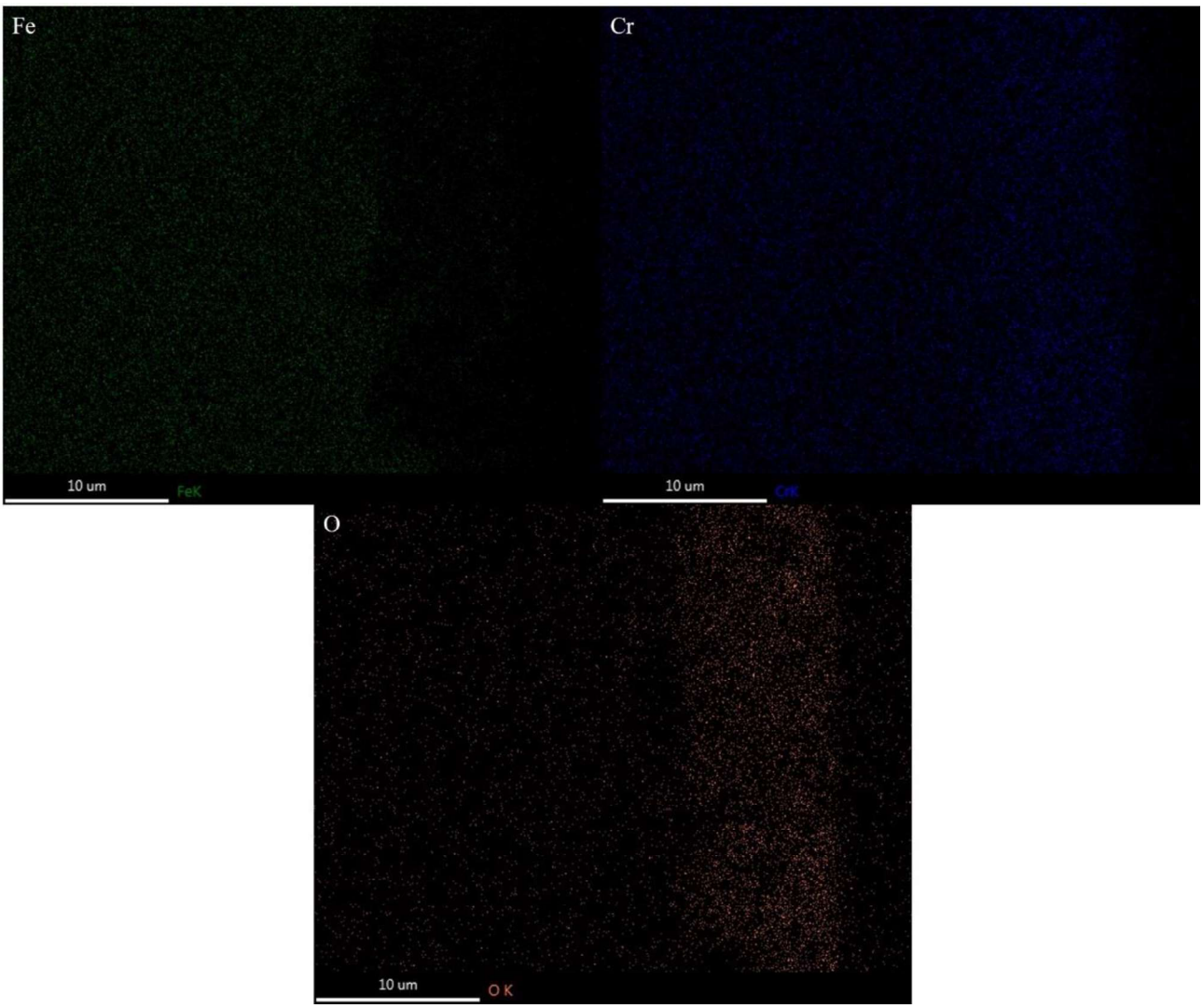
Fe
10 um
FeK
Cr
10 um
CrK
O
10 um
O K

(a)

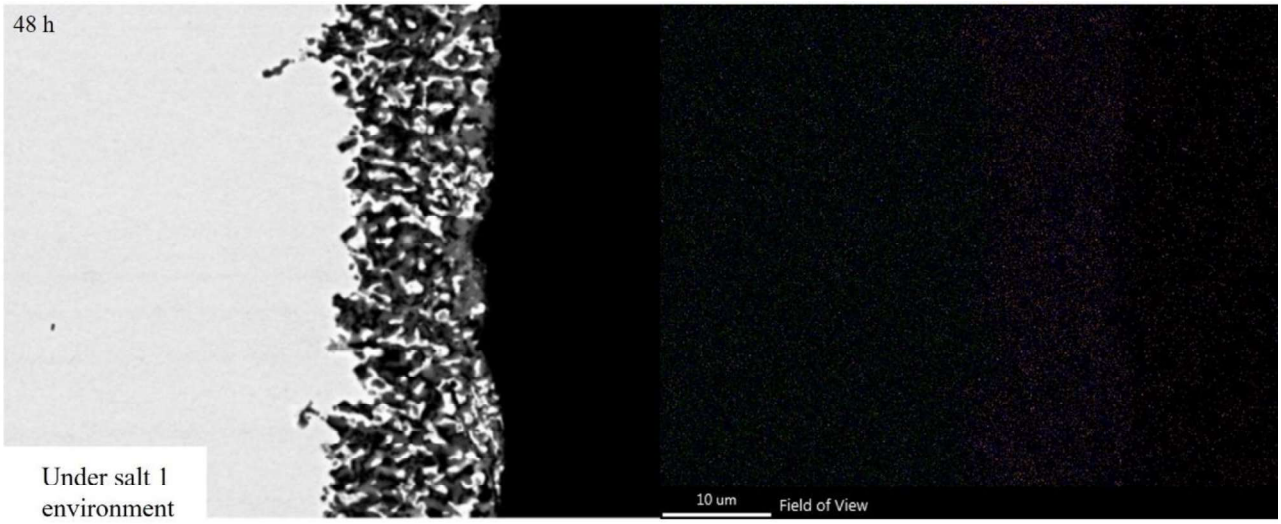
48 h
Under salt 1 environment
10 um
Field of View

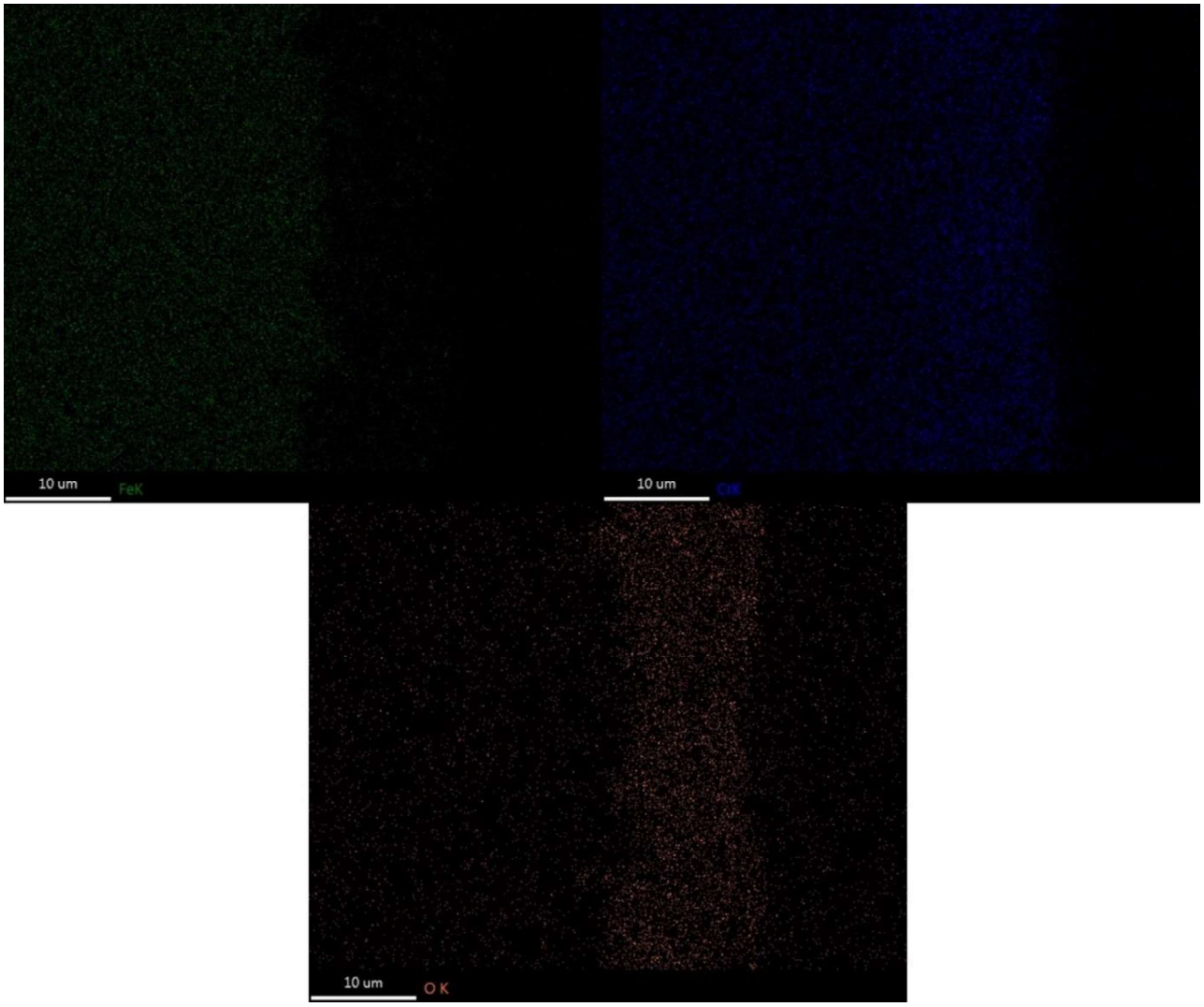

(b)

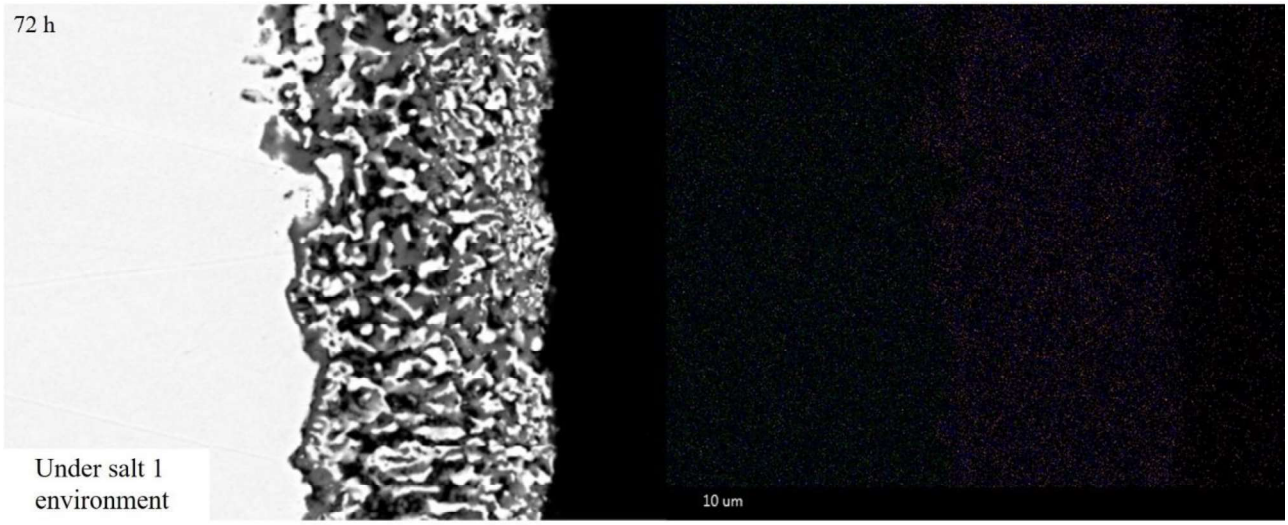

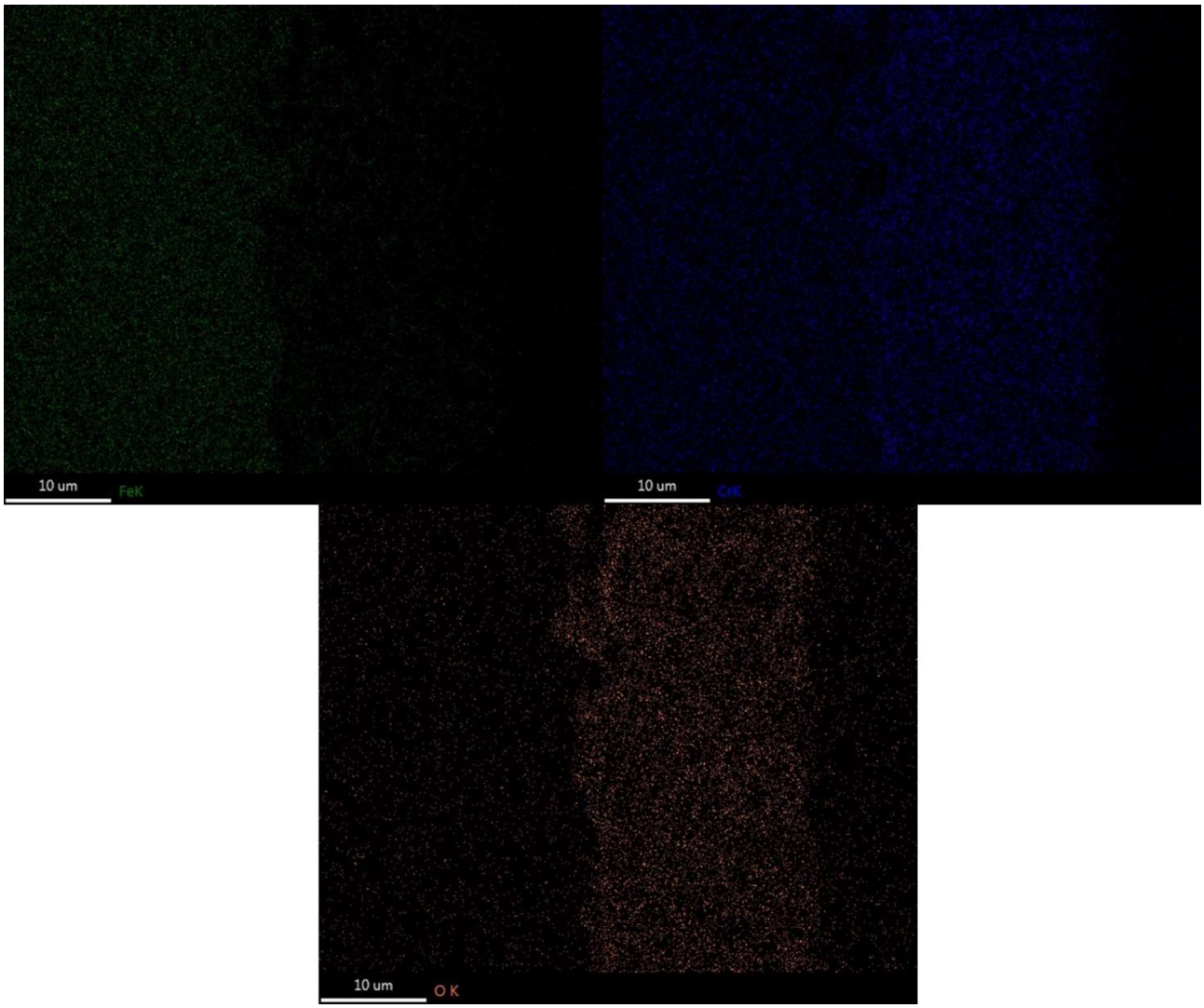

(c)

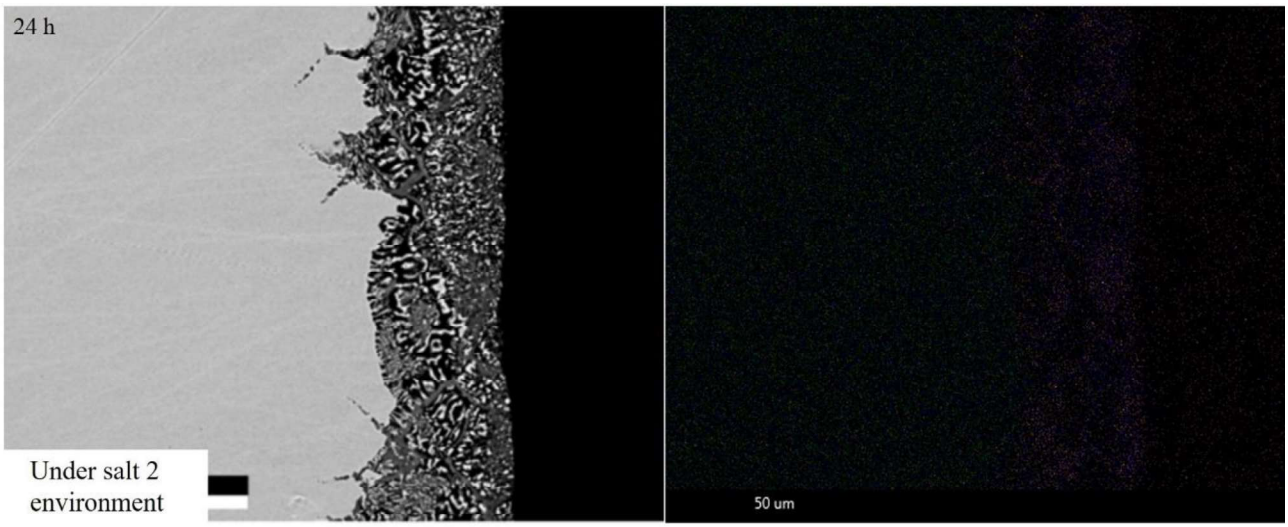

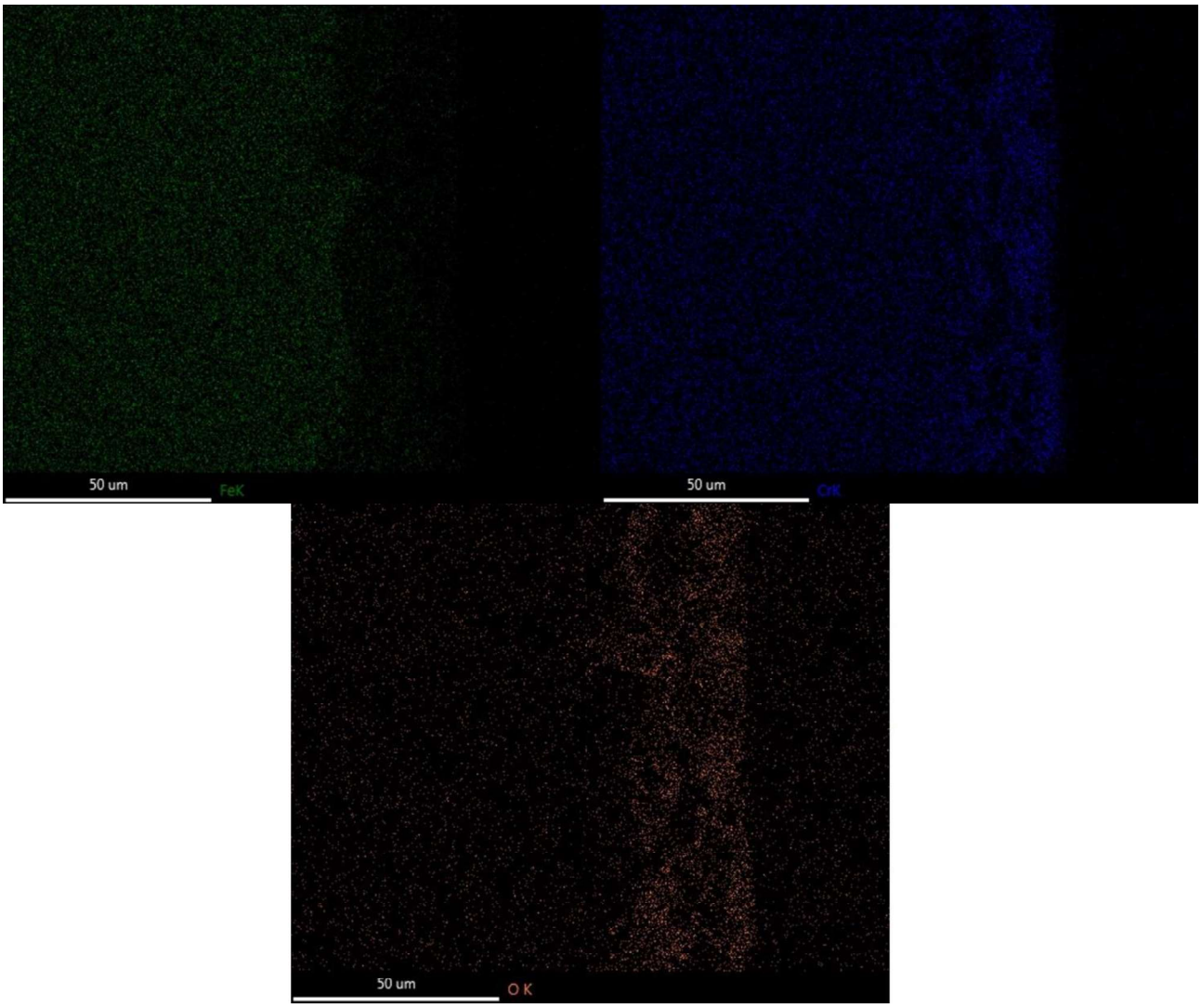
50 um
FeK
50 um
ClK
50 um
O K

(d)

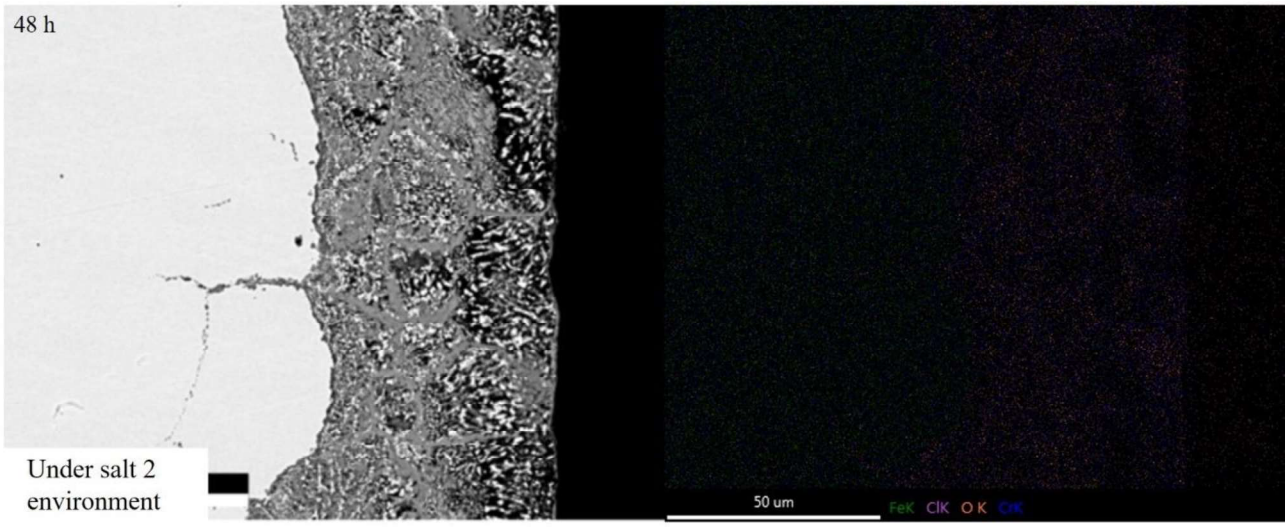
48 h
Under salt 2
environment
50 um
FeK ClK O K ClK

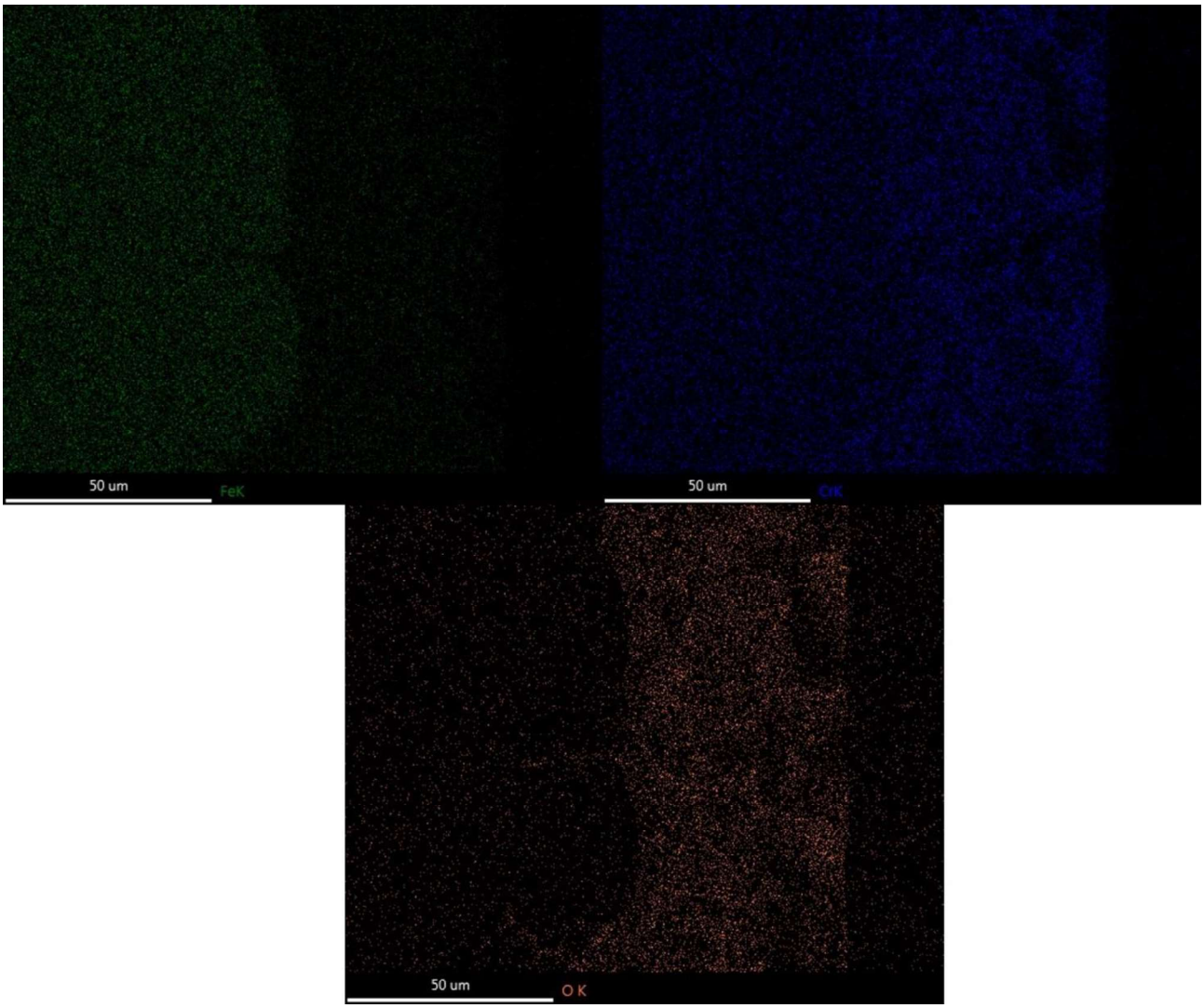

(e)

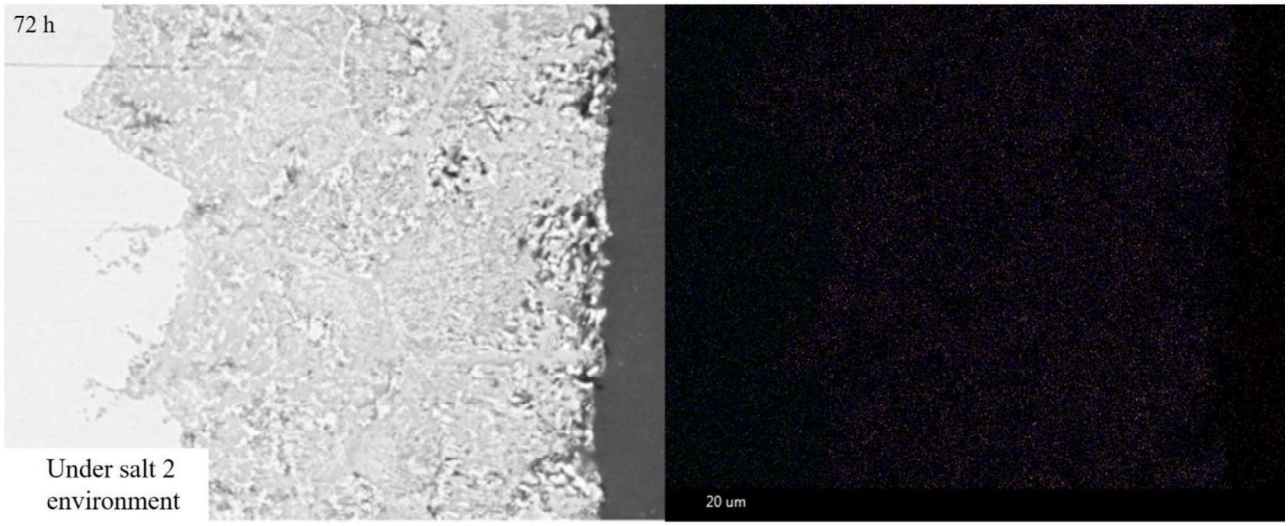

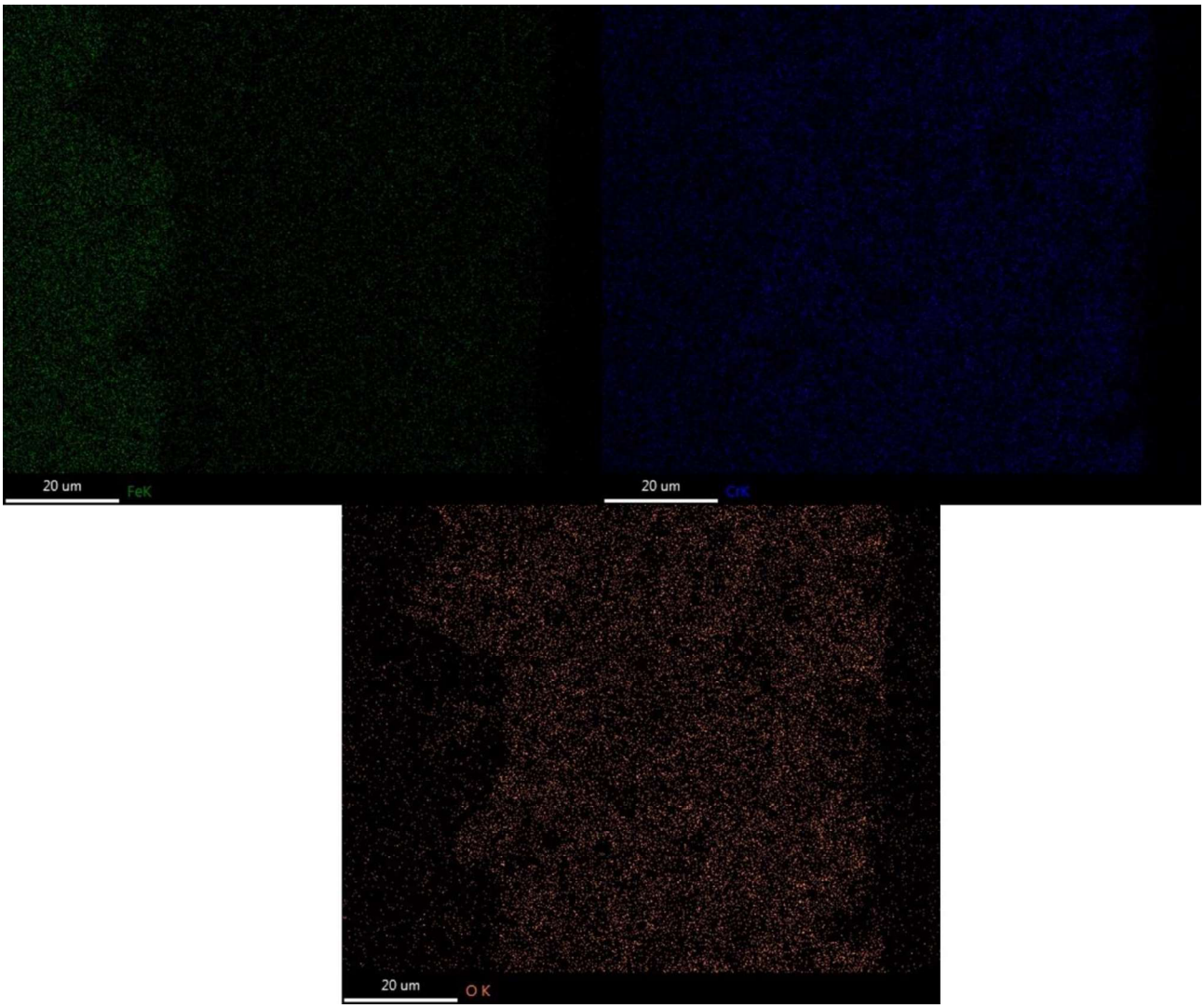

(f)

Fig.10. Cross-sectional SEM images and the elemental distribution of the corroded 316 SS under ternary chloride salts LiCl–KCl–$CaCl_2$ with different compositions after corrosion at 650 ºC for different time. (a) 316 SS corroded for 24 h under salt 1 environment; (b) 316 SS corroded for 48 h under salt 1 environment; (c) 316 SS corroded for 72 h under salt 1 environment; (d) 316 SS corroded for 24 h under salt 2 environment; (e) 316 SS corroded for 48 h under salt 2 environment; (f) 316 SS corroded for 72 h under salt 2 environment.

The corrosion layer is observed by SEM, as shown in Fig.6. The corrosion layer film is thinner in the first 24 h in salt 1 immersion. It can be seen that the corrosion layer with the increase of immersion

time, and the growth rate of corrosion product film decreases after 48 h immersion in both salts. The corrosion layer is a double-layer structure composed of dispersed crystals and an uneven inner corrosion layer [44]. Fig.11 shows the XRD patterns of 316 SS before and after corrosion under LiCl–KCl–$CaCl_2$ with different compositions, to further explore the effects of different components of ternary chloride salts on 316 SS and the corresponding corrosion layer on the average corrosion rate. The characteristic peaks of the original 316 SS at (111), (200) and (220) are clearly visible, indicating that 316 SS has a face-centered cubic (fcc) crystal structure before corrosion under LiCl–KCl–$CaCl_2$. Compared with 316 SS exposed to salt 2, 316 SS exposed to salt 1 has less surface impurities. This also proves that the corrosion strength of salt 2 to 316 SS is much greater than that of salt 1.

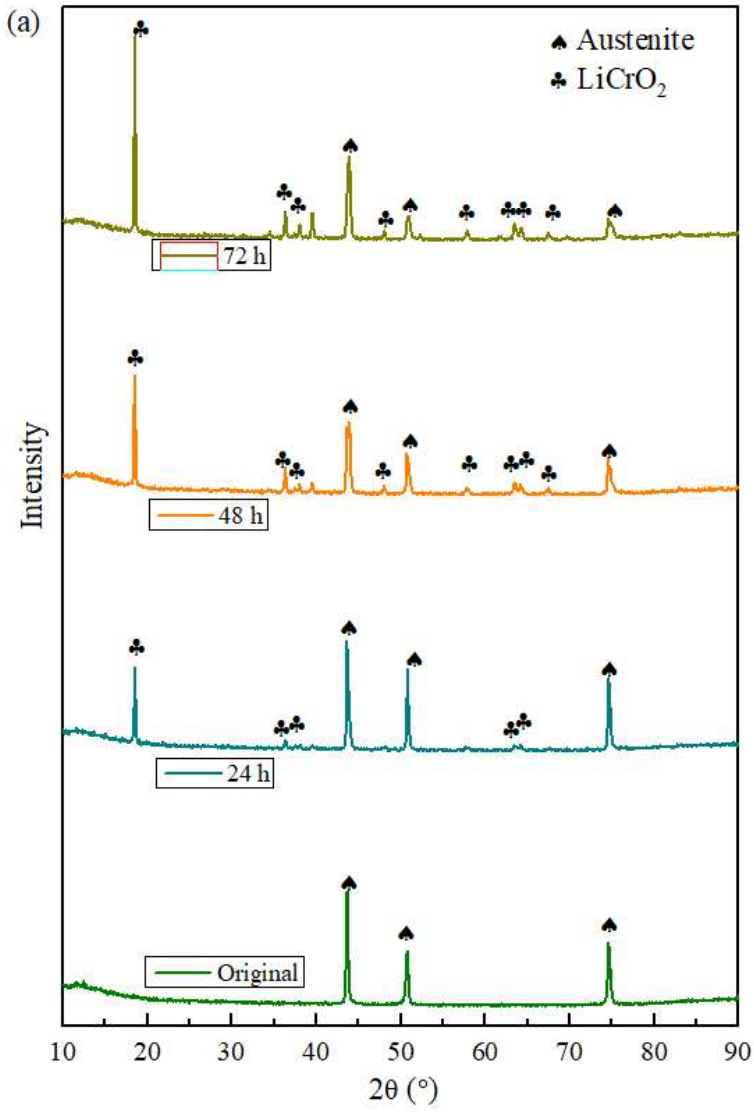
(a)
Austenite
LiCrO2
72 h
48 h
24 h
Original
Intensity
10
20
30
40
50
60
70
80
90
2θ (°)

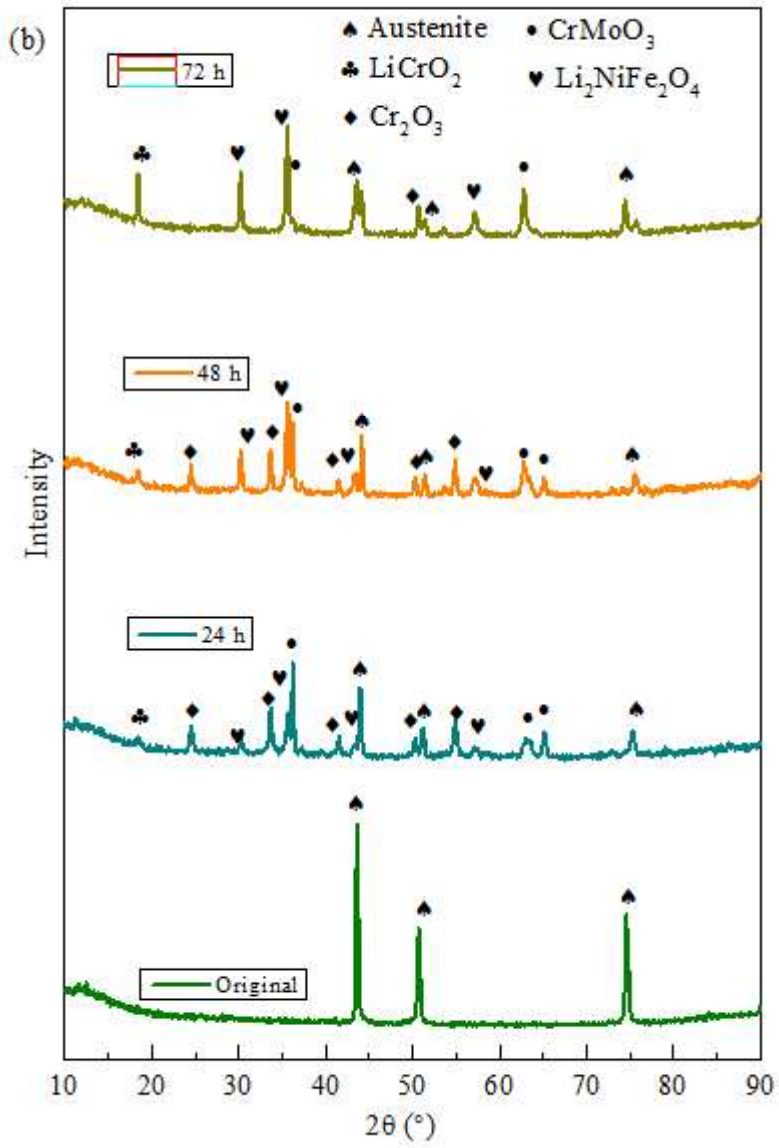

Fig.11. XRD patterns of 316 SS before and after corrosion tested in different ternary chloride salts LiCl–KCl–$CaCl_2$ for different time at 650 ºC. (a) Salt 1 environment; (b) Salt 2 environment.

4.3 Error analysis

To verify the accuracy of the whole experiment, this paper analyzed the error of the experimental results. During the experiment, the standard deviation of melting temperature of ternary chloride salts are calculated as follows [45],

$$S_x = \sqrt{\frac{\sum_{i=1}^{N}(x_i - \bar{x})^2}{N-1}} \quad (15)$$

Further, the standard deviation of the mean value is expressed as,

$$S_{\bar{x}} = \frac{S_x}{\sqrt{N}} \quad (16)$$

where x_i and $\bar{x}$ are the measured values and average values of related paraments, respectively, and N is the number of tests.

In this paper, the error range for the melting temperature of ternary chloride salts during the whole experiment are calculated. The standard deviation range of onset temperature of ternary chloride salts LiCl–KCl–$CaCl_2$ is 0.050-0.985 ºC.

5. Conclusions

The short-term corrosion behavior of 316 SS immersed in ternary chloride salts LiCl–KCl–$CaCl_2$ containing different contents of alkaline earth chloride $CaCl_2$ are investigated experimentally. The kinetics of corrosion layer, the evolution of surface corrosion layer, the chemical and thermal properties of ternary chloride salts LiCl–KCl–$CaCl_2$ before and after corrosion are studied. The following conclusions can be acquired:

(1) 316 SS is immersed in two kinds of ternary chloride salts with different contents of $CaCl_2$. The ternary chloride salts with more $CaCl_2$ show stronger corrosion and faster average corrosion rate. However, with the formation of the outer corrosion layer, the average corrosion rate of 316 SS under the two ternary chloride salts decreases.

(2) When the content of $CaCl_2$ in the ternary chloride salt is high, the ternary chloride salt exhibits strong solubility. The content of Fe-Cr dissolved in chloride in salt 2 with higher $CaCl_2$ content is much higher than that in salt 1. The outer corrosion layer of 316 SS exposed to ternary chloride salt

with higher $CaCl_2$ content is looser. On the contrary, the 316 SS outer corrosion layer exposed to the ternary chloride salt with low $CaCl_2$ content is denser.

(3) At 650 ℃, no new functional groups are formed after corrosion of 316 SS by two ternary chloride salts. However, with the increase of Fe-Cr content in the molten salt, the melting temperature of the two ternary chloride salts decreases. t

Acknowledgements

This work was financially supported by the National Natural Science Foundation of China (Grant No. 52130607, 52090062 and 52211530087) and the Double First-Class Key Program of Gansu Provincial Department of Education (Grant No. GCJ2022-38)

References

[1] C.S. Lai, Y. Jia, L.L. Lai, Z. Xu, M.D. McCulloch, K.P. Wong, A comprehensive review on large-scale photovoltaic system with applications of electrical energy storage, Renewable and Sustainable Energy Reviews 78 (2017) 439-451. https://doi.org/10.1016/j.rser.2017.04.078.

[2] U. Pelay, L. Luo, Y. Fan, D. Stitou, M. Rood, Thermal energy storage systems for concentrated solar power plants, Renewable and Sustainable Energy Reviews 79 (2017) 82-100. https://doi.org/10.1016/j.rser.2017.03.139.

[3] Á.G. Fernández, L.F. Cabeza, Molten salt corrosion mechanisms of nitrate based thermal energy storage materials for concentrated solar power plants: A review, Solar Energy Materials and Solar Cells 194 (2019) 160-165. https://doi.org/10.1016/j.solmat.2019.02.012.

[4] C. Villada, W. Ding, A. Bonk, T. Bauer, Engineering molten MgCl2–KCl–NaCl salt for high-temperature thermal energy storage: Review on salt properties and corrosion control strategies, Solar Energy Materials and Solar Cells 232 (2021) 111344. https://doi.org/10.1016/j.solmat.2021.111344.

[5] W. Ding, T. Bauer, Progress in Research and Development of Molten Chloride Salt Technology for Next Generation Concentrated Solar Power Plants, Engineering 7 (2021) 334-347. https://doi.org/10.1016/j.eng.2020.06.027.

[6] H. Tian, W. Wang, J. Ding, X. Wei, Thermal performance and economic evaluation of NaCl–CaCl2 eutectic salt for high-temperature thermal energy storage, Energy 227 (2021) 120412. https://doi.org/10.1016/j.energy.2021.120412.

[7] Q. Liu, H. Xu, H. Yin, N. Li, W. Wang, L. Li, Z. Tang, Y. Qian, Corrosion behaviour of 316 stainless steel in NaCl-KCl-MgCl2 salt vapour at 700°C, Corrosion Science 194 (2022) 109921. https://doi.org/10.1016/j.corsci.2021.109921.

[8] B. Liu, X. Wei, W. Wang, J. Lu, J. Ding, Corrosion behavior of Ni-based alloys in molten NaCl-CaCl2-MgCl2 eutectic salt for concentrating solar power, Solar Energy Materials and Solar Cells 170 (2017) 77-86. https://doi.org/10.1016/j.solmat.2017.05.050.

[9] B.A. Pint, J.W. McMurray, A.W. Willoughby, J.M. Kurley, S.R. Pearson, M.J. Lance, D.N. Leonard, H.M. Meyer, J. Jun, S.S. Raiman, R.T. Mayes, Re-establishing the paradigm for evaluating halide salt compatibility to study commercial chloride salts at 600°C–800°C, Materials and Corrosion 70 (2019) 1439-1449. https://doi.org/10.1002/maco.201810638.

[10] W. Ding, J. G. Vidal, A. Bonk, T. Bauer, Molten chloride salts for next generation CSP plants: Electrolytical salt purification for reducing corrosive impurity level, Solar Energy Materials and Solar Cells 199 (2019) 8-15. https://doi.org/10.1016/j.solmat.2019.04.021.

[11] A.G. Fernández, J. G. Vidal, E. Oró, A. Kruizenga, A. Solé, L.F. Cabeza, Mainstreaming commercial CSP systems: A technology review, Renewable Energy 140 (2019) 152-176. https://doi.org/10.1016/j.renene.2019.03.049.

[12] J. W. Wang, C. Z. Zhang, Z. H. Li, H. X. Zhou, J. X. He, J. C. Yu, Corrosion behavior of nickel-based superalloys in thermal storage medium of molten eutectic NaCl-MgCl2 in atmosphere, Solar Energy Materials and Solar Cells 164 (2017) 146-155. https://doi.org/10.1016/j.solmat.2017.02.020.

[13] S. Ren, Y. Chen, X. X. Ye, L. Jiang, S. Yan, J. Liang, X. Yang, B. Leng, Z. Li, Z. Chen, Z. Dai, Corrosion behavior of carburized 316 stainless steel in molten chloride salts, Solar Energy 223 (2021) 1-10. https://doi.org/10.1016/j.solener.2021.05.057.

[14] C. C. Tsaur, J.C. Rock, C. J. Wang, Y. H. Su, The hot corrosion of 310 stainless steel with pre-coated NaCl/Na2SO4 mixtures at 750°C, Materials Chemistry and Physics 89 (2005) 445-453. https://doi.org/10.1016/j.matchemphys.2004.10.002.

[15] X. Li, L. Chang, C. Liu, B. Leng, X. Ye, F. Han, X. Yang, Effect of thermal aging on corrosion behavior of type 316H stainless steel in molten chloride salt, Corrosion Science 191 (2021) 109784. https://doi.org/10.1016/j.corsci.2021.109784.

[16] Y. Wang, X. Li, N. Li, C. Ling, Z. Tang, Z. Li, Thermal transport and storage performances of NaCl–KCl–NaF eutectic salt for high temperatures latent heat, Solar Energy Materials and Solar Cells 218 (2020) 110756. https://doi.org/10.1016/j.solmat.2020.110756.

[17] Z. Xu, X. Wei, J. Lu, J. Ding, W. Wang, Simulation of corrosion behavior of Fe–Cr–Ni alloy in binary NaCl–CaCl2 molten salt using a cellular automata method, Solar Energy Materials and Solar Cells 231 (2021) 111301. https://doi.org/10.1016/j.solmat.2021.111301.

[18] H. Sun, P. Zhang, J. Wang, Effects of alloying elements on the corrosion behavior of Ni-based alloys in molten NaCl-KCl-MgCl2 salt at different temperatures, Corrosion Science 143 (2018) 187-199. https://doi.org/10.1016/j.corsci.2018.08.021.

[19] H. Sun, J. Wang, Z. Li, P. Zhang, X. Su, Corrosion behavior of 316SS and Ni-based alloys in a

ternary NaCl-KCl-MgCl2 molten salt, Solar Energy 171 (2018) 320-329. https://doi.org/10.1016/j.solener.2018.06.094.

[20] H. Li, X. Yang, X. Yin, X. Wang, J. Tang, J. Gong, Effect of Chloride Impurity on Corrosion Kinetics of Stainless Steels in Molten Solar Salt for CSP Application: Experiments and Modeling, Oxidation of Metals 95 (2021) 311-332. https://doi.org/10.1007/s11085-021-10025-y.

[21] B.P. Mohanty, D.A. Shores, Role of chlorides in hot corrosion of a cast Fe–Cr–Ni alloy. Part I: Experimental studies, Corrosion Science 46 (2004) 2893-2907. https://doi.org/10.1016/j.corsci.2004.04.013.

[22] J. W. Wang, H. X. Zhou, C. Z. Zhang, W. N. Liu, B. Y. Zhao, Influence of MgCl2 content on corrosion behavior of GH1140 in molten NaCl-MgCl2 as thermal storage medium, Solar Energy Materials and Solar Cells 179 (2018) 194-201. https://doi.org/10.1016/j.solmat.2017.11.014.

[23] W.Y. Zhou, Y. Yang, G.Q. Zheng, K.B. Woller, P.W. Stahle, A.M. Minor, M.P. Short, Proton irradiation-decelerated intergranular corrosion of Ni-Cr alloys in molten salt, NATURE COMMUNICATIONS 11 (2020). https://doi.org/10.1038/s41467-020-17244-y.

[24] W. Ding, H. Shi, Y. Xiu, A. Bonk, A. Weisenburger, A. Jianu, T. Bauer, Hot corrosion behavior of commercial alloys in thermal energy storage material of molten MgCl2/KCl/NaCl under inert atmosphere, Solar Energy Materials and Solar Cells 184 (2018) 22-30. https://doi.org/10.1016/j.solmat.2018.04.025.

[25] Y.S. Li, M. Spiegel, S. Shimada, Corrosion behaviour of various model alloys with NaCl–KCl coating, Materials Chemistry and Physics 93 (2005) 217-223. https://doi.org/10.1016/j.matchemphys.2005.03.015.

[26] K. Sridharan, T. R. Allen, 12 - Corrosion in Molten Salts, Molten Salts Chemistry (2013) 241-

267. https://doi.org/10.1016/B978-0-12-398538-5.00012-3.

[27] H. Ai, J. Hou, X. X. Ye, C.L. Zeng, H. Sun, X. Li, G. Yu, X. Zhou, J. Q. Wang, Influence of graphite-alloy interactions on corrosion of Ni-Mo-Cr alloy in molten fluorides, Journal of Nuclear Materials 503 (2018) 116-123. https://doi.org/10.1016/j.jnucmat.2018.03.001.

[28] H. Yin, J. Qiu, H. Liu, W. Liu, Y. Wang, Z. Fei, S. Zhao, X. An, J. Cheng, T. Chen, P. Zhang, G. Yu, L. Xie, Effect of CrF3 on the corrosion behaviour of Hastelloy-N and 316L stainless steel alloys in FLiNaK molten salt, Corrosion Science 131 (2018) 355-364. https://doi.org/10.1016/j.corsci.2017.12.008.

[29] L. Guo, Q. Liu, H. Yin, T.J. Pan, Z. Tang, Excellent corrosion resistance of 316 stainless steel in purified NaCl-MgCl2 eutectic salt at high temperature, Corrosion Science 166 (2020) 108473. https://doi.org/10.1016/j.corsci.2020.108473.

[30] A.G. Fernández, L.F. Cabeza, Corrosion monitoring and mitigation techniques on advanced thermal energy storage materials for CSP plants, Solar Energy Materials and Solar Cells 192 (2019) 179-187. https://doi.org/10.1016/j.solmat.2018.12.028.

[31] K. Vignarooban, X. Xu, K. Wang, E.E. Molina, P. Li, D. Gervasio, A.M. Kannan, Vapor pressure and corrosivity of ternary metal-chloride molten-salt based heat transfer fluids for use in concentrating solar power systems, Applied Energy 159 (2015) 206-213. https://doi.org/10.1016/j.apenergy.2015.08.131.

[32] M. Sarvghad, S. Delkasar Maher, D. Collard, M. Tassan, G. Will, T.A. Steinberg, Materials compatibility for the next generation of Concentrated Solar Power plants, Energy Storage Materials 14 (2018) 179-198. https://doi.org/10.1016/j.ensm.2018.02.023.

[33] L. Ma, C. Zhang, Y. Wu, Y. Lu, C. Ma, Dynamic corrosion behavior of 316L stainless steel in

quaternary nitrate-nitrite salts under different flow rates, Solar Energy Materials and Solar Cells 218 (2020) 110821. https://doi.org/10.1016/j.solmat.2020.110821.

[34] S. Zhang, H. Li, Z. Jiang, B. Zhang, Z. Li, J. Wu, H. Feng, H. Zhu, F. Duan, Chloride- and sulphate-induced hot corrosion mechanism of super austenitic stainless steel S31254 under dry gas environment, Corrosion Science 163 (2020) 108295. https://doi.org/10.1016/j.corsci.2019.108295.

[35] A. Soleimani Dorcheh, R.N. Durham, M.C. Galetz, Corrosion behavior of stainless and low-chromium steels and IN625 in molten nitrate salts at 600°C, Solar Energy Materials and Solar Cells 144 (2016) 109-116. https://doi.org/10.1016/j.solmat.2015.08.011.

[36] V. Ignatiev, A. Surenkov, I. Gnidoy, A. Kulakov, V. Uglov, A. Vasiliev, M. Presniakov, Intergranular tellurium cracking of nickel-based alloys in molten Li, Be, Th, U/F salt mixture, Journal of Nuclear Materials 440 (2013) 243-249. https://doi.org/10.1016/j.jnucmat.2013.05.001.

[37] Y. Zhao, M. Ren, Y. Shang, J. Li, S. Wang, W. Zhai, G. Zheng, K. Dai, C. Liu, C. Shen, Ultra-sensitive and durable strain sensor with sandwich structure and excellent anti-interference ability for wearable electronic skins, Composites Science and Technology 200 (2020) 108448. https://doi.org/10.1016/j.compscitech.2020.108448.

[38] Z. Zhang, X. Lu, Y. Yan, T. Wang, The dehydration of MgCl2·6H2O by inhibition of hydrolysis and conversion of hydrolysate, Journal of Analytical and Applied Pyrolysis 138 (2019) 114-119. https://doi.org/10.1016/j.jaap.2018.12.014.

[39] H. Sun, J. Q. Wang, Z. Tang, Y. Liu, C. Wang, Assessment of effects of Mg treatment on corrosivity of molten NaCl-KCl-MgCl2 salt with Raman and Infrared spectra, Corrosion Science 164 (2020) 108350. https://doi.org/10.1016/j.corsci.2019.108350.

[40] H. Zhang, F. He, T. Wang, G. Chen, Insights into the interaction of CaCl2 and potato starch:

Rheological, structural and gel properties, International Journal of Biological Macromolecules 220 (2022) 934-941. https://doi.org/10.1016/j.ijbiomac.2022.08.135.

[41] M. Lee, O. Muránsky, I. Karatchevtseva, H. Huang, K.J. Laws, Corrosion performance of Ni-based structural alloys for applications in molten-salt based energy systems: Experiment & numerical validation, Corrosion Science 190 (2021) 109607. https://doi.org/10.1016/j.corsci.2021.109607.

[42] J. Qiu, D.D. Macdonald, R. Schoell, J. Han, S. Mastromarino, J.R. Scully, D. Kaoumi, P. Hosemann, Electrochemical study of the dissolution of oxide films grown on type 316L stainless steel in molten fluoride salt, Corrosion Science 186 (2021) 109457. https://doi.org/10.1016/j.corsci.2021.109457.

[43] Y. Wang, Q. Liu, X. Su, H. Yin, Z. Tang, Corrosion behaviors and protective layer stabilization mechanism of 316 stainless steel in NaCl–KCl–NaF reciprocal salts at high temperatures, Corrosion Science 211 (2023) 110893. https://doi.org/10.1016/j.corsci.2022.110893.

[44] X. Yue, Y. Ren, L. Huang, S. Zou, L. Zhang, Y. Hua, The role of Cl- in the formation of the corrosion products and localised corrosion of 15Cr martensite stainless steel under an CO2-containing extreme oilfield condition, Corrosion Science 194 (2022) 109935. https://doi.org/10.1016/j.corsci.2021.109935.

[45] X. Xu, G. Dehghani, J. Ning, P. Li, Basic properties of eutectic chloride salts NaCl-KCl-ZnCl2 and NaCl-KCl-MgCl2 as HTFs and thermal storage media measured using simultaneous DSC-TGA, Solar Energy 162 (2018) 431-441. https://doi.org/10.1016/j.solener.2018.01.067.

Table captions

Table 1. The component of ternary chloride salts LiCl–KCl–$CaCl_2$, melting points and thermal stabilities of the two salts.

Table 2. Chemical compositions of 316 SS (wt.%).

Table 3. Mass loss of 316 SS after corrosion, average corrosion rate and equivalent corrosion depth of 316 SS under different components for different time.

Table 4. The content of Fe-Cr element before and after corrosion 316 SS.

Table 5. Temperature variation of the ternary chloride salts LiCl–KCl–$CaCl_2$ before and after corrosion.

Figure captions

Fig.1. Apparatus of the static immersion test.

Fig.2. Macro-morphologies of 316 SS after corrosion conducted at 650 ºC for different time.

Fig.3. Mass loss of 316 SS immersed in different component ternary chloride salts LiCl–KCl–$CaCl_2$ for different time.

Fig.4. The average corrosion rate of 316 SS in different compositions of ternary chloride salt LiCl–KCl–$CaCl_2$ at different times.

Fig.5. The equivalent corrosion depth of 316 SS.

Fig.6. SEM images of the corroded 316 SS in ternary chloride salts LiCl–KCl–$CaCl_2$ with different content of $CaCl_2$ at 650 ºC for different time.

Fig.7. Macro-morphologies of ternary chloride salts before and after corrosion conducted at 650 ºC for different time.

Fig.8. IR spectra of individual chloride salt and ternary chloride salts LiCl–KCl–$CaCl_2$ with different

compositions after corrosion.

Fig.9. Melting temperatures of ternary chloride salts..

Fig.10. Cross-sectional SEM image and the elemental distribution of the corroded 316 SS under ternary chloride salts LiCl–KCl–$CaCl_2$ with different compositions after corrosion at 650 ºC for different time.

Fig.11. XRD patterns of 316 SS before and after corrosion testing in different ternary chloride salts LiCl–KCl–$CaCl_2$ for different time at 650 ºC.